



# Built-in electric field boosted exciton dissociation in sulfur doped BiOCl with abundant oxygen vacancies for transforming the pathway of molecular oxygen activation

Chenyu Zhang<sup>a,b,1</sup>, Yaocheng Deng<sup>c,1</sup>, Qiongfang Wan<sup>a,b</sup>, Hao Zeng<sup>c</sup>, Hou Wang<sup>a,b</sup>, Hanbo Yu<sup>d,e</sup>, Haoliang Pang<sup>a,b</sup>, Wei Zhang<sup>a,b</sup>, Xingzhong Yuan<sup>a,b</sup>, Jinhui Huang<sup>a,b,\*</sup>

<sup>a</sup> College of Environmental Science and Engineering, Hunan University, Changsha 410082, PR China

<sup>b</sup> Key Laboratory of Environmental Biology and Pollution Control, Hunan University, Ministry of Education, Changsha 410082, PR China

<sup>c</sup> College of Environment and Ecology, Hunan Agricultural University, Changsha 410082, PR China

<sup>d</sup> School of Hydraulic and Environmental Engineering, Changsha University of Science & Technology, Changsha 410114, PR China

<sup>e</sup> Key Laboratory of Dongting Lake Aquatic Eco-Environmental Control and Restoration of Hunan Province, Changsha 410114, PR China

## ARTICLE INFO

### Keywords:

Sulfur-doped BiOCl  
Molecular oxygen activation  
Built-in electric field  
Exciton dissociation  
CIP degradation

## ABSTRACT

The reactive oxygen species (ROS) generated by photoinduced molecular oxygen ( $O_2$ ) activation has attracted great attention in environmental remediation and pollution control. Herein, we establish a facile sulfur doping strategy that promotes the activation of molecular oxygen over BiOCl for rapid and continuous degradation of organic pollutants. In this work, we demonstrate that the significantly enhanced built-in electric field (BIEF) induced by the heterogeneous introduction of S atoms not only multiplies the electron concentration in the BiOCl matrix, but also accelerates the rapid separation/transfer of charge carriers and inhibits recombination. Driven by this, the exciton behavior in the BOC undergoes a transformation. The electrons generated through exciton dissociation activate the adsorbed  $O_2$  on the surface into superoxide radicals ( $\bullet O_2^-$ ). Benefited from the superior  $O_2$  activation efficiency, the degradation rate constant of ciprofloxacin (CIP) the fabricated S-doped BiOCl increased by 8.8 times, under visible light. This work proposes a strategy to promote the photocatalytic  $O_2$  activation via tuning BIEF and manipulating excitonic effects, which affords new perspective for understanding the reaction mechanisms related to charge transfer in photocatalytic systems.

## 1. Introduction

Semiconductor-based photocatalysis, as a typical photoexcitation process, has shown great prospects in solving the energy crisis and environmental decontamination [1,2]. The development of high-performance semiconductor materials is a decisive factor in improving photocatalytic efficiency. In the mainstream view of multitudinous studies, the process of photocatalytic degradation of pollutants typically involves the separation of photogenerated charge carriers (i.e., electrons and holes) by photoexcitation and subsequent migration to surface sites [3,4]. Molecular oxygen ( $O_2$ ) is a vital component of photochemical processes that occur on photocatalytic materials. On the one hand, molecular oxygen acts as a scavenger of photogenerated electrons to inhibit charge carrier recombination [5,6]. On the other

hand, photoelectron-mediated  $O_2$  activation can produce different reactive oxygen species (ROS) to facilitate the reactions of organic pollutant degradation, mainly including  $\bullet O^-$ ,  $\bullet O_2^-$ ,  $H_2O_2$ ,  $\bullet OH$ , or  $^1O_2$  [7–9]. The nature differences among ROS determine that they will attack different sites on pollutant molecules, resulting in intermediate products with different environmental toxicity. In the deep oxidation process of persistent organic pollutants,  $\bullet O_2^-$ , compared to  $^1O_2$ , is not easy to produce more harmful intermediate products, which is more advantageous during treatment [10,11]. Especially for fluoroquinolone agents, the reaction dominated by  $^1O_2$  is difficult to achieve effective mineralization, while the attack of  $\bullet OH$  will produced more toxic intermediates [12]. Hence, the regulation of  $O_2$  activation pathway to generate specific ROS (i.e.,  $\bullet O_2^-$ ) is of great significance for guiding the safe removal of contaminants.

\* Corresponding author at: College of Environmental Science and Engineering, Hunan University, Changsha 410082, PR China.

E-mail address: [huangjinhui@hnu.edu.cn](mailto:huangjinhui@hnu.edu.cn) (J. Huang).

<sup>1</sup> Chenyu Zhang and Yaocheng Deng contributed equally to this work.

Weakening the O–O bond is a reliable strategy for O<sub>2</sub> activation, which requires sufficiently efficient separation and transfer of charge carriers in the photocatalyst [13]. In this regard, one of the effective strategies is to shorten the transport/diffusion distance of bulk photo-generated carriers in photocatalysts through two-dimensional (2D) engineering. Unfortunately, 2D semiconductors bulk with giant excitonic effect will generate plenty of energetic photoinduced products, namely excitons, during the photoexcitation process [14,15]. Neutral excitons are bound electron-hole pairs formed by attractive Coulomb interactions, and their differences and correlations with charge carriers dramatically affect the photocatalytic O<sub>2</sub> activation behavior, especially for low dimensional semiconductors [16]. The vigorous interaction among excitons have a competitive effect on the generation of charge carriers in photocatalytic process, which is detrimental to the formation of ROS mediated by photoelectrons [17,18]. Therefore, it is particularly critical to weaken the excitonic effect to promote the dissociation of excitons into free charge carriers in practical environmental pollution control. Notably, such excitonic effect has been neglected in most of the reported works regarding photocatalytic applications.

Bismuth oxyhalides (BiOX, X = Br, I, Cl), as a class of typically layered 2D ternary oxides, has attracted much attention in photocatalytic applications [19]. The distinctive built-in electric field (BIEF) can be formed between the layered structures composed of alternating [Bi<sub>2</sub>O<sub>2</sub>] slabs and double [X] slabs in BiOX, which is generally considered beneficial for the separation of photogenerated charge carriers and shortening the transport distance. In 2017, Wang et al. revealed the exciton behavior in BiOBr material with confined layered structure [20]. The following year, their group regulated the dissociation of excitons into charge carriers in BiOBr via O<sub>vs</sub> [21]. Recently, Zhang's group introduced more surface O<sub>vs</sub> on BiOCl and BiOBr through surface boron doping strategies, while also weakening the strong excitonic effect in the samples, thereby promoting exciton dissociation [11,22]. It has been proven that excitons prefer to dissociate in regions with disordered energy distribution [23,24]. The relevant regulation strategies include order-disorder interfaces construction [25], defects introduction [21, 26–28], metal ion coordination [18,29], doping [22,30], and heterojunction engineering [31,32]. Without sacrificing the stability of catalysts, oxygen vacancies (O<sub>vs</sub>) introducing and elemental doping are the most direct and widespread strategies used to promote O<sub>2</sub> activation as well as exciton dissociation. To the best of our knowledge, there are few targeted investigations that combine the BIEF with exciton dissociation in the reported works so far, especially in nonmetal-doped BIOX [11,22, 33–35]. First, defects and doping can break the balance of electronic structure, inducing the dissociation of excitons. Secondly, surface O<sub>vs</sub> can endow materials with superior O<sub>2</sub> adsorption capacity to produce activated ROS effortlessly. Furthermore, the BIEF in the photocatalysts is enhanced under the action of both above, manifested as the promotion of charge carrier separation and transfer efficiency. Accordingly, it is expected to regulate the exciton effect through BIEF, achieving the accumulation of electron concentration and improving the production performance of charge-transfer-mediated ROS.

It has been reported that sulfur doping was successfully improve photogenerated carrier separation/transfer and ROS generation toward BiOX materials [35,36]. The S atoms doped into BiOX will substitute halogen atoms, endowing material with interesting structural and performance changes [33]. Inspired by the above, we propose herein a facile strategy to weaken the inherent excitonic effect brought about by the 2D layered structure of BiOCl by sulfur incorporating. The heterogeneous S atoms inserted into interlayer space increases the content of surface O<sub>vs</sub> in BiOCl and induces interlayer polarization to tune BIEF. The findings exhibit that the enhanced BIEF promotes the excitons to dissociate more easily into charge carriers, while suppressing the recombination of charge carriers. To this end, combined with density functional theory (DFT) calculations, we delved into the effects of sulfur doping on the BIEF strength, O<sub>2</sub> activation performance, exciton behavior, and the degradation performance of various pollutants over

BiOCl. Interestingly, the O<sub>2</sub> activation behavior in BiOCl alters dramatically due to the introduction of S: the ROS generation pathway is converted from <sup>1</sup>O<sub>2</sub> (energy-transfer-mediated) over the pristine BiOCl into •O<sub>2</sub> (charge-transfer-mediated) over the S-doped BiOCl. Such specific ROS production behavior can effectively achieve harmless degradation of CIP. This work provides new points of view for the performance advancement of photocatalysts by modulating the behavior of BIEF and excitons in low dimensional semiconductors.

## 2. Experimental section

### 2.1. Materials

All chemicals used were analytical reagent grade and purchased from commercial suppliers without further purification unless otherwise mentioned. All solutions were prepared in ultrapure 18.25 MΩ·cm Milli-Q water (Millipore).

### 2.2. Preparation of Samples

S-doped BiOCl samples were prepared following previous reports with some minor modifications [37]. In a typical synthesis procedure, 4 mmol Bi(NO<sub>3</sub>)<sub>3</sub>·5 H<sub>2</sub>O and 4 mmol KCl were dispersed uniformly in 60 mL ethylene glycol (EG) under stirring for 30 min to form a homogeneous and colorless solution. Subsequently, a certain amount (0, 1, 2, 3, 4 mmol) of thiourea as sulfur source was added into the above mixture under vigorous stirring. After further stirring for 30 min, the precursor solution was transferred into a 100 mL Teflon-lined autoclave and heated for 12 h at 160 °C. The products were collected by centrifugation, washed with distilled water and absolute ethanol for three times to neutral pH, and finally dried under vacuum at 60 °C for 10 h. According to the different dosage of thiourea, the obtained samples were labeled as BOC or SBOC-x (x = 1, 2, 3 and 4).

### 2.3. Characterizations

Powder X-ray diffraction (XRD) patterns were measured on Bruker D8A A25 X X-ray diffractometer with Cu Kα radiation source. The Fourier transform infrared (FTIR) spectra were acquired on Thermo Scientific Nicolet iS20 in the range of 4000–400 cm<sup>−1</sup> with a resolution of 4 cm<sup>−1</sup> to identify the surface functional groups. The microstructure and element distribution of the samples were studied by scanning electron microscopy (SEM) on ZEISS Sigma 300 coupled with energy-disperse X-ray spectrometry (EDX). High-resolution transmission electron microscopy (HRTEM) images were acquired by a JEM-F200 transmission electron microscope (Japan) operated at an acceleration voltage of 300 kV. X-ray photoelectron spectroscopy (XPS) data were obtained on a Thermo Scientific ESCALAB Xi+ with an Al Kα radiation. The N<sub>2</sub> adsorption-desorption isotherms of the samples were collected at 77 K using Micromeritics ASAP 2460 system. The UV-Vis diffuse reflectance spectroscopy (DRS) was performed on Shimadzu UV-3600 instrument with an integrating sphere attachment from 200 to 800 nm, referenced to BaSO<sub>4</sub>. The surface potential of samples was measured on Bruker Dimension Iconin atomic force microscope (AFM) with Kelvin probe mode. The Shimadzu TOCVCPH analyzer was used to investigate the mineralization ability of samples. The Nano ZS90 zeta potential analyzer was employed to determine zeta potential of samples. Electron paramagnetic resonance (EPR) (Bruker EMX PLUS) was used to investigate the reactive species generated during the experiment.

Steady-state prompt fluorescence (PF), steady-state phosphorescence (PH), time-resolved fluorescence decay spectra (TRPF) and time-resolved phosphorescence decay spectra (TRPH) were obtained on a steady-state and time-resolved Fluorescence Spectrometers (FLS-1000, Edinburgh Instruments). The excitation wavelengths of all spectra were 260 nm. The average lifetimes were fitted by the following exponential Eqs. (1, 2):

$$I_{(t)} = I_0 + A_1 \exp(-t/\tau_1) + A_2 \exp(-t/\tau_2) + A_3 \exp(-t/\tau_3) \quad (1)$$

$$\tau_{\text{ave}} = \tau_1 \times I_1 + \tau_2 \times I_2 + \tau_3 \times I_3 \quad (2)$$

Where  $I_0$  is the baseline correction value,  $A_1$ ,  $A_2$  and  $A_3$  are the pre-exponential factors,  $\tau_1$ ,  $\tau_2$  and  $\tau_3$  are the lifetime (ns) in different photoprocesses, and  $\tau_{\text{ave}}$  represents the average lifetime.

## 2.4. Molecular oxygen activation measurements

A 20  $\mu\text{L}$  aliquot of an aqueous suspension of the sample (5 mg/mL) and 20  $\mu\text{L}$  of 3,3',5,5'-tetramethylbenzidine (TMB) (50 mM aqueous solution) were dispersed in 2 mL of HAc/NaAc buffer solution (0.6 M: 0.2 M). The mixture was illuminated after the adsorption and desorption equilibrium by employing a 300 W Xe lamp with a 420 nm cutoff filter as light source. To evaluate the oxidation of TMB molecules, the mixture was taken at different time intervals for UV-vis spectrophotometer, monitored at 370 nm. The measurements were also performed under various atmospheres to research molecular oxygen activation properties. The type of active oxygen species was verified by scavenger tests adding different amounts of scavengers prior to the UV-vis measurements a (UV-2700, SHIMADZU Corporation, Japan): (i) 200  $\mu\text{L}$  of 100 mM mannite; (ii) 200  $\mu\text{L}$  of 2000 unit/mL catalase (CAT); (ii) 100  $\mu\text{L}$  of 5000 unit/mL superoxide dismutase (SOD); (iv) 5 mg carotene.

## 2.5. Photocatalytic activity test

All experiments were carried out in triplicate for a given condition. The photocatalytic activity of S-doped BiOCl samples was evaluated using CIP as target pollutant under visible light irradiation (Beijing Perfectlight, PLS-SXE300D/300DUV,  $\lambda > 420 \text{ nm}$ ). In a typical batch test, 20 mg of the sample was added into a quartz vessel containing 50 mL CIP aqueous solution at a concentration of CIP (10 mg  $\text{L}^{-1}$ ). Before illumination, the suspension was kept stirring in the dark for 30 min to ensure adsorption-desorption equilibrium. At predetermined time intervals, 1 mL aliquot was collected and filtrated through 0.22  $\mu\text{m}$  filter membrane for further analysis. The photo-degradation efficiency of CIP was measured by high-performance liquid chromatography (HPLC). The test procedure for other pollutants was the same as above. The radical capture experiments were conducted as the similar program mentioned-above with certain amounts of scavengers, in which EDTA-2Na (10 mM), furfuryl alcohol (FFA) (5 mM), isopropanol (IPA) (5 mM), *p*-benzoquinone (*p*-BQ) (10 mM) were added as scavengers of holes ( $\text{h}^+$ ), singlet oxygen ( $^1\text{O}_2$ ), hydroxyl radical ( $\bullet\text{OH}$ ), and superoxide radical ( $\bullet\text{O}_2^-$ ), respectively.

## 2.6. Analytical methods

The quantitative analysis of pollutants was performed using a HPLC (1260 series; Agilent Technologies) with a C18 column and ultraviolet detection (UV) detector. The eluent programs and detection wavelengths were: (i) 0.1% formic acid- $\text{H}_2\text{O}$  and acetonitrile (80:20 v/v) with  $\lambda = 278 \text{ nm}$  for CIP and (50:50 v/v) with  $\lambda = 273 \text{ nm}$  for bisphenol A (BPA), (ii) 0.1% oxalic acid- $\text{H}_2\text{O}$  and acetonitrile (73.5:26.5 v/v) with  $\lambda = 352 \text{ nm}$  for tetracycline hydrochloride (TC) and (iv) 0.1% acetic acid- $\text{H}_2\text{O}$  and methanol (47.5:52.5 v/v) with  $\lambda = 264 \text{ nm}$  for sulfamethoxazole (SMX). Photocatalytic generation of  $\bullet\text{O}_2^-$  and  $^1\text{O}_2$  was studied with nitro blue tetrazolium (NBT) and furfuryl alcohol (FFA) under visible light irradiation, respectively. Refer to the detailed experiment procedure in Text S3.

ESR trapping of  $^1\text{O}_2$  and  $\bullet\text{O}_2^-$  was conducted using the standard spin trap 2,2,6,6-tetramethylpiperidine (TEMP) and 5,5-dimethyl-1-pyrroline-N-oxide (DMPO), respectively. Specifically, a 50  $\mu\text{L}$  amount of an aqueous suspension of samples (10 g  $\text{L}^{-1}$ ) was mixed with 0.5 mL of TEMP (50 mM) aqueous solution or DMPO in methanol. After being

illuminated for 10 min, the mixture was characterized using a Bruker EMX plus model spectrometer operating at room temperature.

## 2.7. Photoelectrochemical measurements

Photocurrent measurement was completed in the standard three-electrode system through CHI 760E electrochemical workstation (Chenhua Instrument, China), in which photocatalyst-coated FTO was used as the working electrode, Pt plate as the counter electrode, and Ag/AgCl as the reference electrode. The electrolyte was a 0.5 M  $\text{Na}_2\text{SO}_4$  solution. A 300 W xenon lamp with a visible-light cutoff filter ( $>420 \text{ nm}$ ) was used as the light source. The as-fabricated catalyst (10 mg) was added into 100  $\mu\text{L}$  of Nafion and 1 mL of ethanol mixture. Subsequently, a 40  $\mu\text{L}$  of the above suspension was uniformly dropped onto the surface of a FTO plate and dried at room temperature, with the exposed area of the electrode was 0.49  $\text{cm}^2$ . The photoresponsive signals of the samples were measured under chopped illumination. Electrochemical impedance spectra (EIS) were carried out in a frequency range from  $1^{-1}$  to  $10^5 \text{ Hz}$ . The frequency of the Mott Schottky plots was 1 kHz.

## 2.8. DFT calculations

the corresponding electron density differences were calculated using the Vienna ab initio simulation package (VASP) [38,39]. The electron exchange and associated energy were treated in the Perdew-Burke-Ernzerhof (PBE) generalized gradient approximation (GGA) as functions [40]. The spin polarization was considered in the calculations. The DFT-D corrections were crucial in determining noncovalent forces by the Grimme scheme. For all structures, the cutoff energy was 400 eV, and the integration in the Brillouin zone was performed on a  $3 \times 3 \times 1$  k-point grid sampled with the Monkhorst-Pack45 scheme [41]. For the calculation of possible catalytic pathways, the convergence tolerances were set as follows: the energy was  $1 \times 10^{-5} \text{ eV atom}^{-1}$ , the maximal force was 0.03 eV  $\text{\AA}^{-1}$ .

# 3. Results and discussion

## 3.1. Morphologies and Physicochemical Characterizations

The microscopic morphology and structural changes of the pristine BOC and as-prepared SBOC materials are directly observed through SEM. As can be seen from Fig. 1a-e, sulfur doping content has an enormous influence on the morphology of BOC. Obviously, the pristine BOC showed a microsphere structure assembled from the radical growth of highly dense nanosheets (about 10 nm thick), ranging in size from 0.5 to 1  $\mu\text{m}$  (Fig. 1a). With the doping of sulfur, the structure of BOC first disintegrated into nanoplates with a transverse size of about 5.5  $\mu\text{m}$  (Fig. 1b). This may be because the strong interaction between  $\text{S}^{2-}$  and  $\text{Bi}^{3+}$  inhibits the growth of nanocrystals, affecting the stacking of positive  $[\text{Bi}_2\text{O}_2]$  slabs and double negative  $[\text{Cl}]$  slabs. As the content increases, the nanoplates further shrunk in size and became more porous, then re-interweave (Fig. 1c). Interestingly, when the thiourea was added to 3 mmol, it was first observed that the surface of the interlaced nanoplates gradually collapsed, forming microspheres wrapped in a large number of fragments. Subsequently, a dragon fruit-like structure consisted of loose nanoplates gradually emerged (Fig. 1d and Fig. S1a). It is expected that this rigorously hierarchical nanostructure provided abundant interpenetrating channels to expose more active sites and facilitate charge transport. When the addition of thiourea was further increased to 4 mmol (Fig. 1e and Fig. S1b), the surface nanoplates transform into flower-like structures. Such a significant difference in morphology is due to the intense and continuous nucleation-dissolution-recrystallization mechanism caused by the introduction of sulfur [42,43]. Furthermore, EDX mapping images display the uniform distribution of S, Bi, O, Cl over SBOC-3, demonstrating the successful introduction of S atoms (Fig. S2). Nitrogen



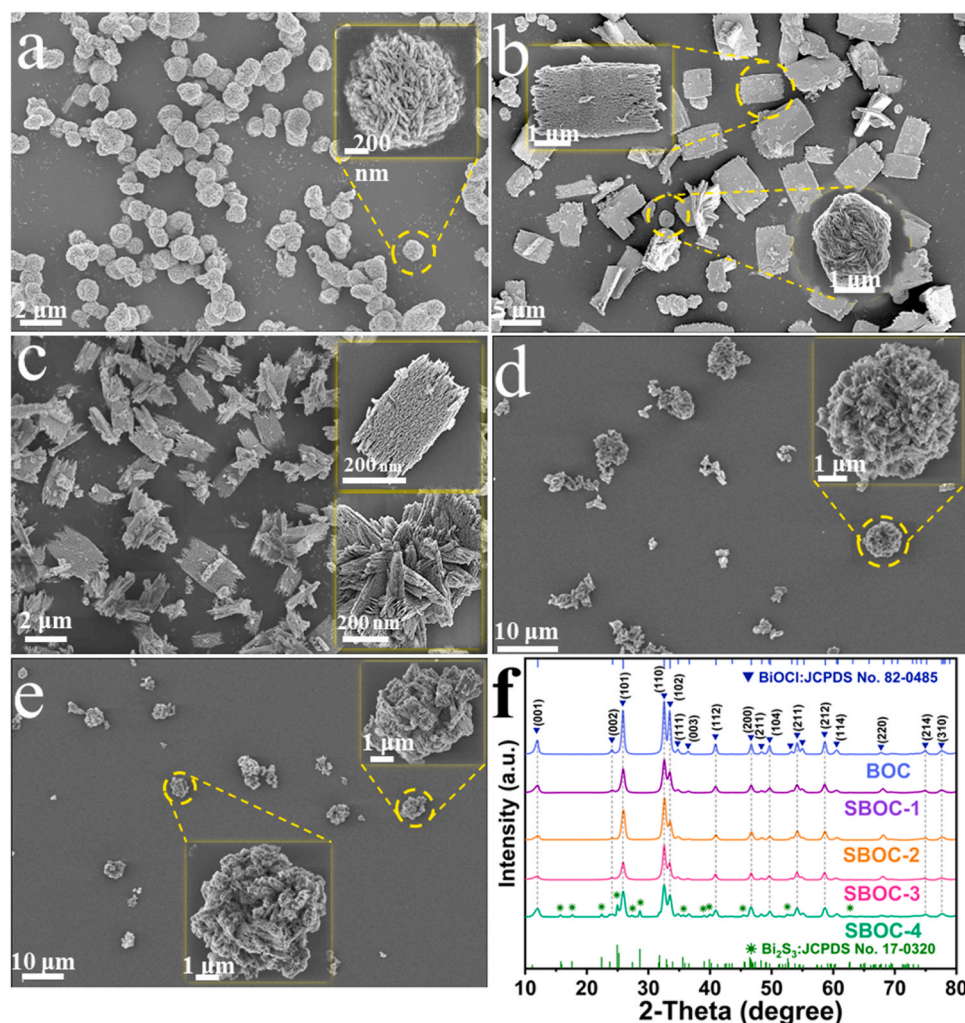


Fig. 1. SEM images of (a) BOC, (b) SBOC-1, (c) SBOC-2, (d) SBOC-3, and (e) SBOC-4. (f) XRD patterns of BOC and SBOC-x samples.

adsorption-desorption isotherm measurements were performed to further characterize the specific surface area and pore size distribution of the samples. As shown in Fig. S3, both the BOC and SBOC-3 displayed type IV curves with a H3 typical hysteresis cycle, which were coincident with the mesoporous structure. The measured BET surface area of SBOC-3 is  $57.6665 \text{ m}^2 \text{ g}^{-1}$ , which was higher than  $32.3623 \text{ m}^2 \text{ g}^{-1}$  of BOC sample (Table S1). This phenomenon is consistent with the situation observed by SEM.

The structure of as-prepared samples was further investigated via XRD, as shown in Fig. 1f. Except for SBOC-4, the obtained photocatalysts could be well-indexed to tetragonal BiOCl with lattice parameters of  $a = b = 3.887 \text{ \AA}$  and  $c = 7.354 \text{ \AA}$  (JCPDS No. 82-0485), and there were no impurity peaks. With the increase of S doping amount, the peak intensity decreased slightly. Obviously, a certain amount of S doping does not lead to the significant phase transition of BOC crystals. The atomic ( $0.7807 \text{ \AA}$ ) and ionic radius ( $0.184 \text{ \AA}$ ) of Cl is actually very similar to those of S ( $0.8738 \text{ \AA}$  and  $0.181 \text{ \AA}$ ), respectively [44,45]. These results suggested that the doping of S is like halogen mixing. It could be inferred that  $\text{S}^{2-}$  has replaced  $\text{Cl}^-$  and been inserted into the BOC crystalloid. Notably, when the addition of thiourea further enhanced to 4 mmol during synthesis, some characteristic peaks indexed to orthorhombic  $\text{Bi}_2\text{S}_3$  were observed ( $a = 11.149 \text{ \AA}$ ,  $b = 11.304 \text{ \AA}$ , and  $c = 3.981 \text{ \AA}$ ; JCPDS No. 17-0320). Such a phenomenon means that excessive addition of thiourea induces the formation of BiOCl- $\text{Bi}_2\text{S}_3$  composite.

It could be concluded via SEM that the morphology of BOC would change measurably due to excessive doping of sulfur element.

Subsequently, HRTEM images clearly displayed the lattice fringes and the major exposed-facet (001) of BOC and SBOC-3 (Fig. S4). The interplanar spacing of about  $0.276\text{--}0.277 \text{ nm}$  corresponded to the (110) atomic plane of BOC. In comparison, the interplanar spacing of the SBOC-3 sample was slightly larger than the pristine BOC, at  $0.285 \text{ nm}$ . Such a phenomenon indicated that the Cl atoms may have been occupied by S atoms in the interlayer, enlarging the interlayer space. Moreover, structural defects could be clearly seen in the images of SBOC-3 samples. To reveal the influence of S introduction on the surface chemical properties and electronic structure of BOC samples, FTIR and XPS analysis have been conducted. Functional groups on the sample were characterized by FTIR (Fig. 2a). The peaks at around  $517 \text{ cm}^{-1}$  was ascribed to Bi-O stretching [46,47]. Moreover, the addition of thiourea did not appreciably alter the stretching vibration of the Bi-O bond in the samples, which confirmed the structural integrity of the as-prepared samples. The peaks at  $3433$  and  $1614 \text{ cm}^{-1}$  were attributed to the  $\nu(\text{O-H})$  stretching and  $\delta(\text{O-H})$  bending vibrations of the adsorbed  $\text{H}_2\text{O}$  [48,49]. The two new peaks shown at  $1028$  and  $610 \text{ cm}^{-1}$  in SBOC-3 were attributed to the vibration of the Bi-S bond. Notably, the introduction of S induced a significant red-shift in the asymmetric and symmetric stretching vibration peaks of the Bi-Cl band at  $1062 \text{ cm}^{-1}$  of the BOC, accompanied by an increase in peak intensity. This indicated that S atoms may have replaced negative [Cl] interlayer.

XPS analysis was employed to characterize the samples toward further investigating the variations of chemical configuration and oxygen species before and after doping. As shown in Fig. S5a, the presence



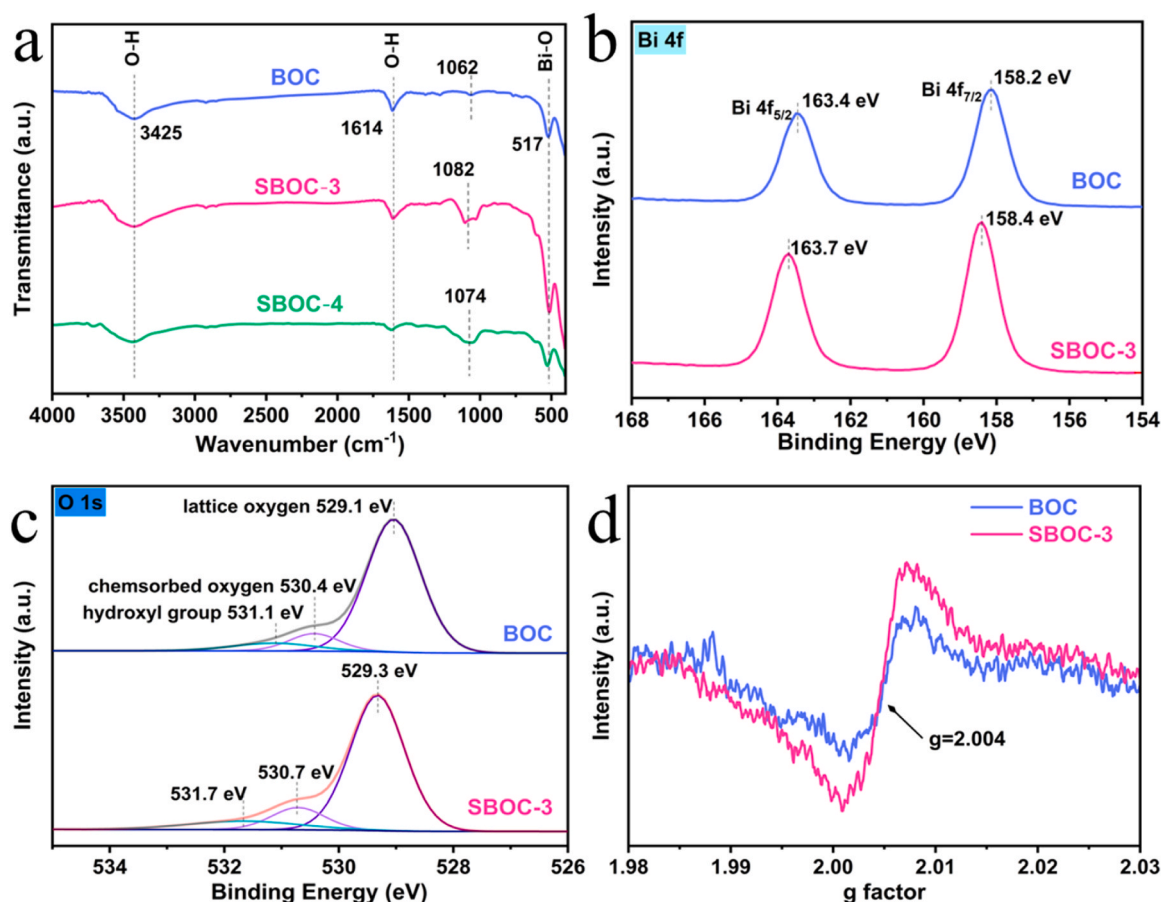


**Fig. 2.** (a) FTIR spectra of BOC, SBOC-3, and SBOC-4. High resolution of XPS spectra (b) and (c) O 1s XPS spectra of BOC and SBOC-3. (d) EPR spectra of BOC and SBOC-3.

of Bi, Cl, and O elements on the surfaces of BOC and SBOC-3 has been demonstrated. Note that the spectral peak of S 2p overlapped with that of Bi 4 f. The high-resolution XPS spectra of SBOC-3 showed that Bi 4 f was deconvoluted into two strong peaks with binding energy of 158.4 and 163.7 eV, respectively attributing to the spin-orbit coupling effect of Bi 4 f<sub>7/2</sub> and Bi 4 f<sub>5/2</sub> of Bi<sup>3+</sup> states (Fig. 2b). Moreover, two peaks of Bi 4 f were shifted toward higher binding energy. This phenomenon indicated that the introduction of S<sup>2-</sup> had changed the chemical environment of BOC and induced the electronic offset from Bi to S by Bi-S bond [33,50]. The Cl 2p spectrum of SBOC-3 is shown in (Fig. S5b), two main peaks with binding energies at 197.1 and 198.8 eV (splitting energy  $\Delta = 1.7$  eV) corresponded to the Cl 2p<sub>3/2</sub> and Cl 2p<sub>1/2</sub> of Cl<sup>-</sup>, respectively. The high binding energies of Cl 2p demonstrated the decrease in the atomic content of Cl, suggesting that the Cl<sup>-</sup> was substituted by S<sup>2-</sup> because of the weakened van der Waals forces (nonbonding interactions) between [Cl...Cl] atoms [51,52]. The substitutional doping often leads to small lattice distortions in the crystal structure, thereby increasing system energy. As identified from the O 1s spectra of SBOC-3 (Fig. 2c), the divided peaks centered at 529.3, 530.7, and 531.7 were assigned to lattice oxygen (Bi-O bond), surface hydroxyl group, and chemisorbed oxygen at O<sub>vs</sub>, respectively [53]. As compared to pristine BOC, the ratio of the chemisorbed oxygen to lattice oxygen in SBOC-3 increased prominently (from 13% to 16%), corroborating more OV formed after the introduction of S, which was conducive to O<sub>2</sub> activation [26]. EPR is sensitive and direct approach to monitor surface O<sub>vs</sub> [54]. As shown in Fig. 2d, SBOC-3 exhibited a stronger EPR signal intensity at g ≈ 2.004 than that of BOC, explicitly demonstrating that there were more O<sub>vs</sub> on the surface of SBOC-3.

### 3.2. Photophysical Properties and Enhanced Built-In Electric Field

The substituted S atoms profoundly affect the morphology and optical properties of the BOC sample. The pristine BOC appeared as a brown powder, and as the doping amount of S increased, the color changed from gray to a terrimus (Fig. S6). This color change intuitively implies the light absorption characteristics of the sample. UV-vis DRS spectra unveiled the optical absorption properties of BOC and SBOC-3, as shown in Fig. 3a. The results demonstrate that each sample had strong response under UV-vis light. Compared with pristine BOC, the absorption edge of SBOC-3 with S doping shifted to longer wavelength, indicating that the visible-light absorption range was improved [55]. As depicted in the inset of Fig. 3a, the calculated  $E_g$  of BOC and SBOC-3 were estimated to be 3.20 and 2.27 eV, respectively. The narrower  $E_g$  is in favor of the incident light absorption and photocarriers generation, exciting more photoelectron and hole pairs [56]. As shown in Fig. 3b, the flat band potentials ( $U_{fb}$ ) of BOC and SBOC-3 investigated by Mott-Schottky (M-S) measurements were -0.26 and -0.36 V (vs. NHE), respectively. Both samples were n-type semiconductors and thermal dynamically activate O<sub>2</sub> for •O<sub>2</sub><sup>-</sup> production. Moreover, the charge carrier density value ( $N_d$ ) was further quantified by M-S plots, the derived  $N_d$  of SBOC-3 was 2.09 times higher than BOC. It can be proposed that the synergistic effect between O-vacancies and IEF induced by S doping remarkably improved the charge separation and transfer ability of BOC material. Based on above data, the potential of valence band ( $E_{VB}$ ) and conduction band ( $E_{CB}$ ) were obtained, as shown in Fig. 3c. The calculation details are listed in the appendix. Especially, the conduction band of both pristine BOC and SBOC-3 catalysts were more negative than the redox potential ( $E_H$  value) of O<sub>2</sub>/•O<sub>2</sub><sup>-</sup> (-0.28 V vs.

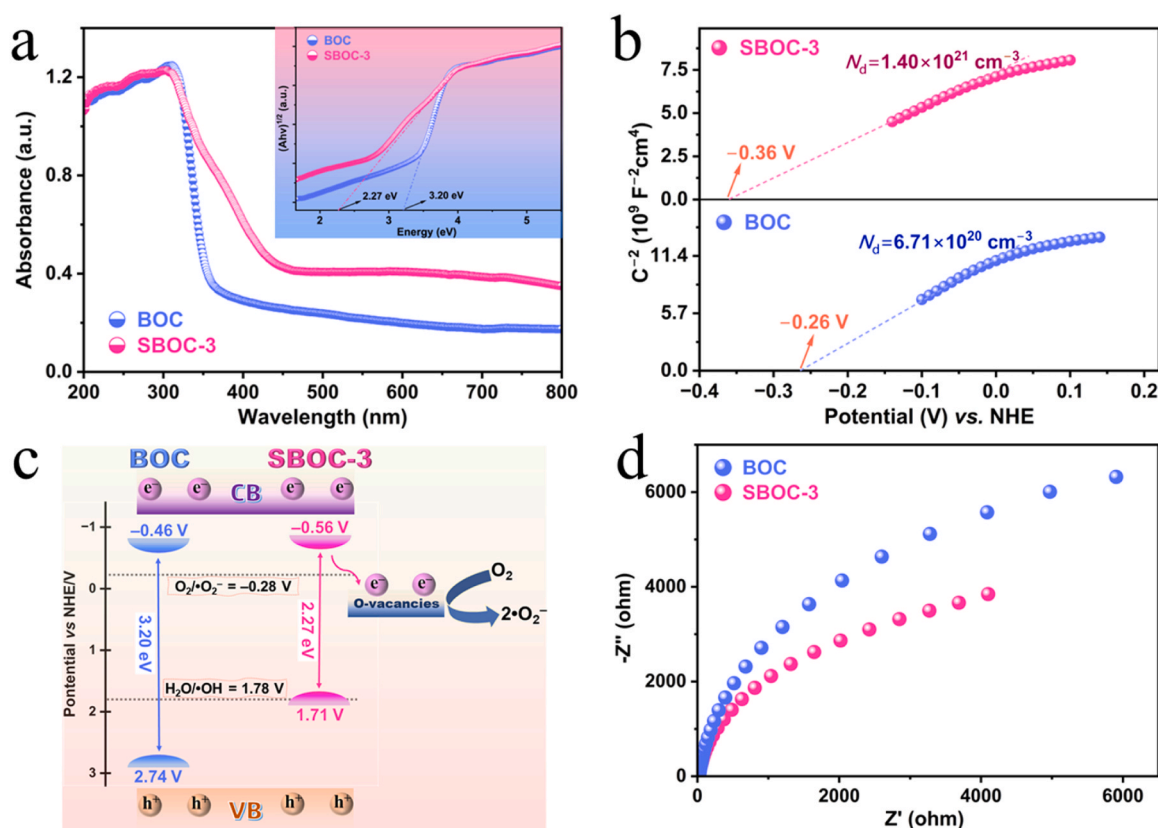


Fig. 3. (a) UV-vis absorption spectra and (b) Mott-Schottky plots with the calculated charge carrier density of BOC and SBOC-3. (c) Band gap alignments of BOC and SBOC-3, with the schematic illustration of the interfacial electron-transfer processes induced by O vacancies. (d) EIS spectra of BOC and SBOC-3.

NHE) [25], indicating the sufficient reduction capacity for  $\cdot\text{O}_2^-$  generation (Fig. 3c). These results suggested that band position could be regulated via the change of element content in BOC.

Moreover, EIS plots were employed to further investigate the migration efficiency of electrons (Fig. 3d). The smaller radius of semicircle arc implies the lower charge transfer impedance at the electrode/electrolyte [57]. Obviously, the semicircle of SBOC-3 was lower than that of BOC, thereby suggesting that the introduction of S atoms could decrease the interfacial charge transfer resistance. BIEF, as the driving force for charge carrier separation and migration, is a dynamic factor affecting photocatalytic performance [58]. The BIEF induced by the polarization among different constituent layers allows electrons and holes to be immediately separated after generation [34]. According to the above results, the insertion of  $\text{S}^{2-}$  ions was expected to induce uneven distribution of interlayer charges, which allowed for fine-tuning of the BIEF. In this regard, the model developed by Kanata et al. was employed to measure the BIEF magnitude for the as-fabricated samples [58,59], where the BIEF intensity was determined by surface potential and surface charge density (details in the Text S4, Supporting Information). The surface potential and surface charge density of samples was measured by Kelvin probe force microscope (KPFM) and Zeta potential, respectively. As shown in Fig. 4a and b, there was a significant difference in surface potential distribution between BOC and SBOC-3 samples, and the surface potential of SBOC-3 ( $\Delta E = 120.54 \text{ mV}$ ) was much higher than that of BOC ( $\Delta E = 73.65 \text{ mV}$ ). As illustrated in Fig. 4c, the surface charge density of SBOC-3 was also enlarged obviously compared with that of BOC. According to the normalization of the calculated results, the SBOC-3 manifested a boosted BIEF intensity, which was 3.10 times higher than that of BOC (Fig. 4d). The above experimental measurements verifies that sulfur doping could regulate the BIEF effectively, favoring the directional separation and transfer of photogenerated charge-carriers.

### 3.3. Photocatalytic ROS generation over SBOC-3

We have found that S doping induces more  $\text{O}_{\text{vs}}$  on the surface of BOC, and the presence of  $\text{O}_{\text{vs}}$  appreciably influence the  $\text{O}_2$  activation behavior in the samples [21]. The enhanced BIEF in SBOC-3 was expected to be accompanied by an increase in the production of ROS mediated by charge transfer. To start with, we employed TMB as a probe molecule to investigate the molecular  $\text{O}_2$  activation performance of BOC before and after S doping. The oxidation of TMB was evaluated by examining the time-dependent revolution of absorbance at 370 nm. As shown in Fig. 5a, the continuous increase in absorbance at the monitoring wavelength clearly suggested that both BOC and SBOC-3 produced ROS, and the latter has superior activation performance. Moreover, the different oxidation rates in various atmosphere demonstrated that the oxidation characteristics of the two samples were highly dependent on  $\text{O}_2$  (Fig. S7). It is worth noting that TMB still underwent slight oxidation in  $\text{N}_2$  atmosphere, possibly because of the presence of  $\text{h}^+$  in the sample [26,60]. To clearly identify the functional ROS involved in TMB oxidation, a variety of scavengers were introduced into the reaction system, in which carotene, mannitol, SOD, and CAT specifically inhibited the production of  $^1\text{O}_2$ ,  $\cdot\text{OH}$ ,  $\cdot\text{O}_2^-$  and  $\text{H}_2\text{O}_2$ , respectively. As depicted in the Fig. 5b, only the addition of SOD could obviously suppress the oxidation of TMB over SBOC-3, while other scavengers have negligible effect on the reaction rate, revealing that  $\cdot\text{O}_2^-$  is the main photogenerated ROS produced by SBOC-3. To further quantitative analysis of  $\cdot\text{O}_2^-$  generation, nitro blue tetrazolium (NBT) was employed as the molecular probe. According to the calculation, the cumulative amount of  $\cdot\text{O}_2^-$  produced by the SBOC-3 sample within five minutes was significantly higher than that of the BOC (Fig. S8). Additionally, Fig. 5c showed that the steady-state concentration of  $\cdot\text{O}_2^-$  photogenerated by BOC and SBOC-3 could be estimated as  $2.09 \times 10^{-5}$  and  $2.30 \times 10^{-4} \text{ M}$ , respectively, and the latter was one order of magnitude higher. By

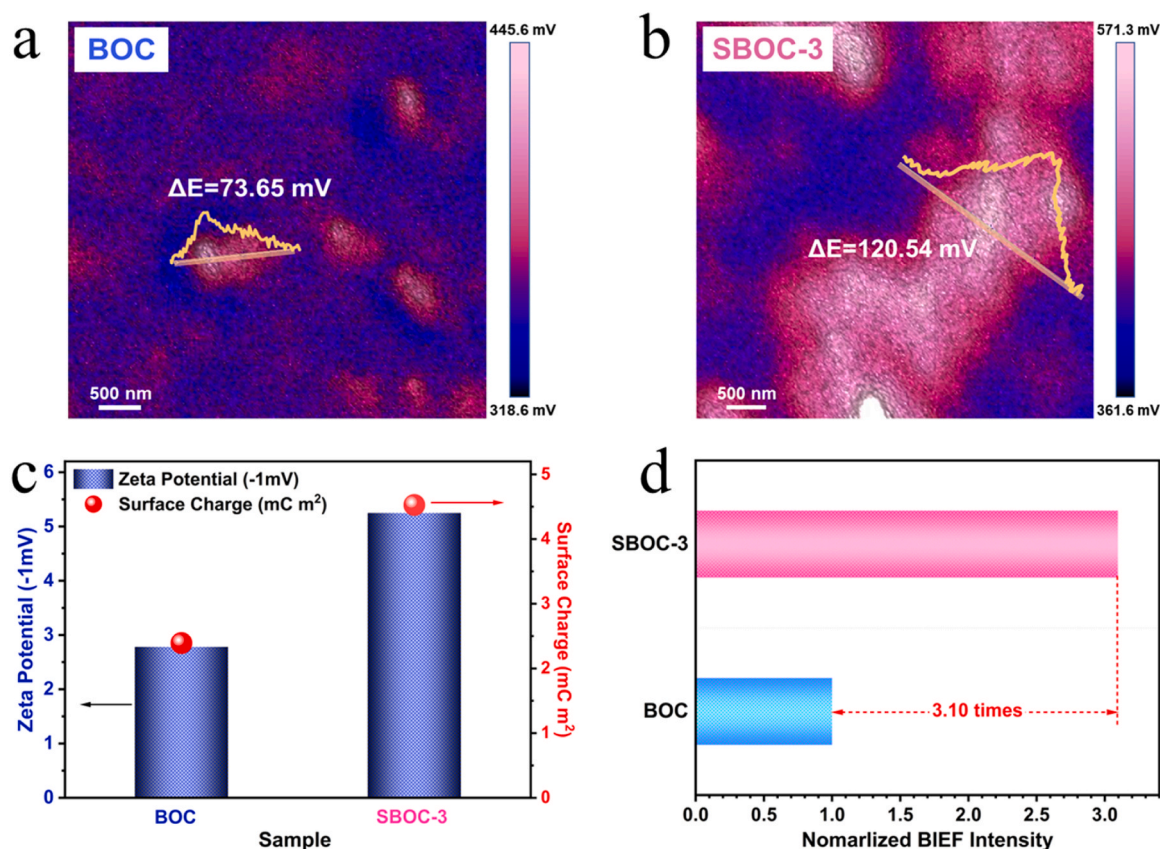


Fig. 4. KPFM images with surface potential of (a) BOC and (b) SBOC-3. (c) Surface charge density of BOC and SBOC-3 calculated by Zeta potential. (d) Comparison of IEF intensity between BOC and SBOC-3 (normalizing the intensity of BOC to be “1”).

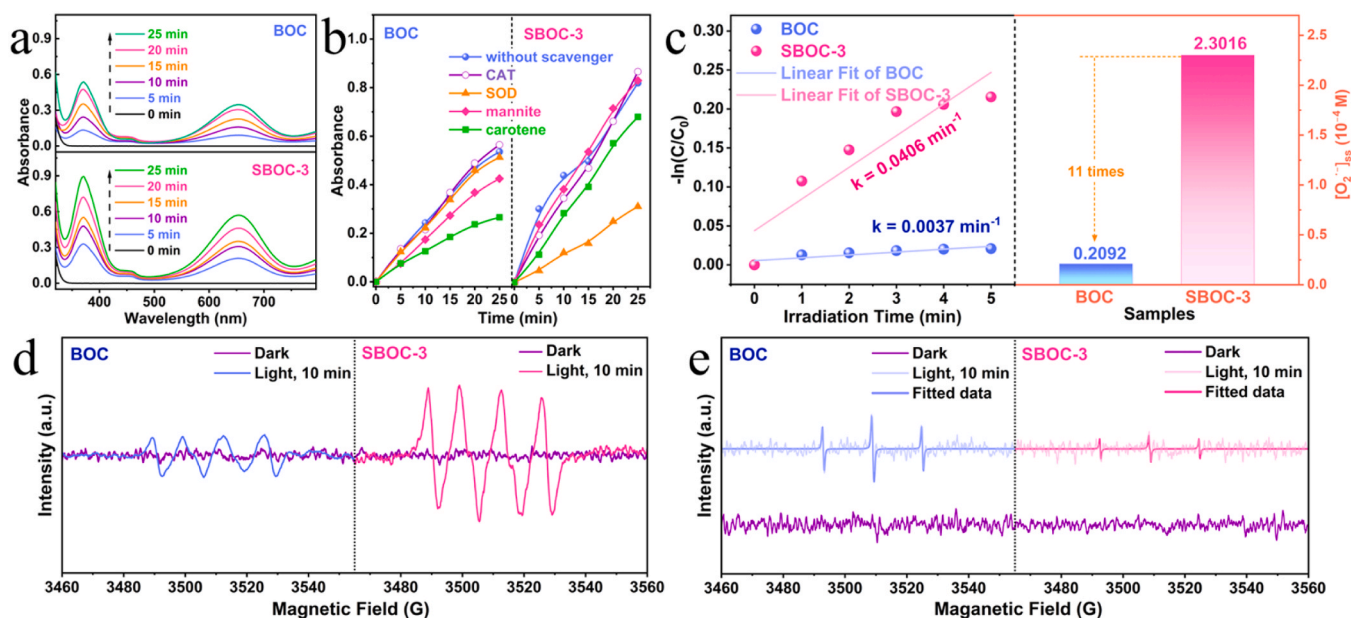


Fig. 5. (a) Time-dependent absorption spectra and (b) absorbance evolution of TMB oxidation monitored at 370 nm in the presence of different scavengers over BOC and SBOC-3 in air. (c) Photocatalytic NBT decomposition profiles and the corresponding reaction rate constants (left) and steady-state concentration (right) of  $\bullet\text{O}_2^-$  over BOC and SBOC-3. ESR spectra of different samples in the presence of (d) DMPO in methanol and (e) TEMP in water, under visible light irradiation.

contrast,  $^1\text{O}_2$  was the dominant ROS of BOC, indicating its giant excitonic effect [21]. The experiment using FFA to quantify  $^1\text{O}_2$  also confirmed this conclusion (Fig. S9).

The results of EPR measurements were direct evidence for the ROS

identification. DMPO ( $k(\text{DMPO} + \bullet\text{O}_2^-) = 2\text{--}170 \text{ M}^{-1} \text{ sec}^{-1}$ ) in methanol was selected as a trapping agent to identify photogenerated  $\bullet\text{O}_2^-$  [61]. As shown in Fig. 5d, a more intense DMPO- $\bullet\text{O}_2^-$  signal was found in the presence of SBOC-3 sample under irradiation. In sharp contrast, BOC



exhibited negligible signal intensity. Such a phenomenon further demonstrated the enhanced  $\bullet\text{O}_2$  generation with SBOC-3, which agreed with the TMB and NBT experiments. Moreover, TEMP was used to detect the production of  $^1\text{O}_2$  in photocatalytic systems. The signal corresponding to 2,2,6, 6-tetramethylpiperidine-n-Oxyl represented the formation of TMEP- $^1\text{O}_2$  adduct [11,20]. It can be found though fitting that a typical 1:1:1 triplet signal arose in the presence of BOC (Fig. 5e), which was consistent with those of TEMPO. By contrast, a tiny TEMPO signal was exhibited over SBOC-3, which suggested the noteworthy suppression in  $^1\text{O}_2$  photogeneration. These results were mutually corroborated by the probe experiment, clearly proving that the increase of O-vacancies and BIEF induced by S doping remarkably promoted the hot electron-mediated ROS in the BOC system.

Generally, the  $^1\text{O}_2$  production involved the energy transfer process between long-lived excitons and ground state oxygen ( $^3\text{O}_2$ ), while the  $\bullet\text{O}_2^-$  generation depended on the charge transfer process between  $e^-$  and molecular oxygen, with a competitive relationship between the two [62, 63]. According to the dominant species of two sample the accelerated electron transfer (through excitation dissociation) behavior in SBOC-3 has been pointed out [18]. The distinct properties of molecular  $\text{O}_2$  activation between BOC and SBOC-3 suggested that sulfur doping induced unique exciton behavior. According to the TMB experiments above,  $\bullet\text{OH}$  was not produced in the catalytic system of SBOC-3, revealing that the  $^1\text{O}_2$  did not come from the disproportionation of  $\bullet\text{OH}$  (details in SI) [64]. FFA was employed as a chemical probe to further unraveled the dominant mechanism of the involved  $^1\text{O}_2$  generation. As illustrated in Fig. S10, the similar reaction rates in the presence of SOD excluded the potential charge transfer pathways for  $^1\text{O}_2$  generation. It is speculated that the high  $^1\text{O}_2$  yield in BOC system was attributed to the robust excitonic effect caused by the confined layered structure, which inhibited the electron productivity [22]. On the contrary, a simple S doping strategy disrupted the stability of excitons in BOC sample, transforming the pathway of molecular oxygen activation from  $^1\text{O}_2$  to  $\bullet\text{O}_2^-$ .

### 3.4. Mechanism insight into photoinduced excitonic processes

To explicitly unravel the exciton processes in S-doped BiOCl systems, photoluminescence measurements under both ambient and low-temperature conditions were conducted. As shown in Fig. S11, ambient-temperature (300 K) steady-state prompt fluorescence (PF) spectra was first employed, in which BOC and SBOC-3 showed similar characteristic emission of intrinsic interband excitation with an emission peak centered at 419 nm, and the intraband emission at around 551 nm could be assigned to the defect state induced by oxygen vacancies or doping [21,22]. On the one hand, the PF emission originated in radiative decay of singlet excitons in the sample, thus the significant decrease of PF intensity of SBOC-3 revealed the dramatically decreased concentration of singlet excitons. On the other hand, the suppression of  $e^- - h^+$  recombination was also one of the reasons for the attenuation of PF intensity in SBOC-3, meaning that the introduction of S could significantly improve the bulk charge separation (BCS) efficiency through BIEF tuning [34]. The time-resolved PF spectra recorded at corresponding emission peaks over the samples (Fig. S12a) showed that the average radiation lifetime of SBOC-3 at the intrinsic band-edge emission was higher than that of BOC, which was 4.73 ns and 3.09 ns, respectively. This result demonstrated that excitons over SBOC-3 existed in the form of singlet states. By contrast, the corresponding emission peak at  $\text{O}_{\text{vs}}$  exhibited similar average radiation lifetimes, proving the quite distinct relaxation processes of the charge carriers at intrinsic emission and defect emission peaks (Fig. S12b). Subsequently, to elucidate the effect of S doping on exciton dissociation, low-temperature photoluminescence measurements were performed to reduce dark feature and the robust nonradiative relaxation of excitons. The PF spectra recorded at 77 K exhibited a noticeable intensity increase in intrinsic band-edge emission relative to 300 K as well as a red shift due to the radiative

decay of excitons (Fig. 6a). The binding energies ( $E_b$ ) of excitons were calculated according to the redshift of the intrinsic band-edge peak at 77 K relative to 300 K, respectively. Sulfur doping appreciably reduced the  $E_b$  of excitons in BOC from 444 eV to 289 eV, indicating a dramatically suppression of the excitonic process in BOC.

The phosphorescence (PH) is caused by radiation decay from the triplet excited states retransition back to the singlet ground states, which can be used to further explore processes involving excitons and photo-generated charge carriers [65]. PH spectra with longer lifetime are allowed to be extracted from PF spectra with a certain delay time. As shown in Fig. 6b, the weaker PH intensity implied a lower yield of triplet excitons. Besides, the two samples exhibited emission characteristics like the low-temperature PL spectrum over a long delay time of 20 ms, especially the similar intrinsic emission at 498 nm and exciton emission at 692 nm. More importantly, the significant difference between defect state lifetime (ns level) and delay time (ms level) indicated that exciton dissociation mediated by oxygen vacancies was the principal reason for the defect induced emission [21]. Then, time-resolved PH spectra recorded the lifetime of the triplet exciton. The faster decay of the exciton lifetime over SBOC-3 (3.25 ms) compared with BOC (4.28 ms) at 498 nm was consistent with the remarkable prolongation of the photo-generated carrier lifetime (Fig. 6c). The distribution of singlet and triplet excitons in SBOC-3 corroborated that singlet excitons were inclined to dissociate into free electrons and holes rather than convert to  $^1\text{O}_2$ . Subsequently, our DFT calculations of the electronic structures of BOC and SBOC-3 confirmed that excitons tend to dissociate in the disordered energy distribution. As shown in Fig. 6d, the introduction of S atoms and oxygen vacancies in BOC brings about a significant mid-gap state between the valence and conduction bands, which breaks the electron uniformity in the pristine BOC. As a result, excitons in an unstable state will continuously transform into free charge carriers. Based on the above results, the trapping processes involved in SBOC-3 was proposed (Fig. 6e): Before recombining with the hole, the photoexcited electrons initially transitioned from  $E_{\text{VB}}$  to  $E_{\text{CB}}$  through the bandgap and subsequently relax into the deeper  $\text{S-O}_{\text{vs}}$  state instead of the shallow exciton-mediated state. In other words, the introduction of such intermediate bandgap state impeded the direct recombination of holes to electrons. Furthermore, the transient photocurrent response (TPR) was performed to examine the differentiation of photogenerated electrons. Compared with BOC, the increases in photocurrent intensity (Fig. 6f) and electron concentration (Fig. 3b) over SBOC-3 indicated a boosted capability for hot electron generation as well as charge transfer to the surface. Combined with the remarkable enhancement of the BIEF, it was verified that S doped in BOC matrix accelerated exciton dissociation into photogenerated carriers and inhibited the  $e^- - h^+$  recombination.

### 3.5. Evaluation of photocatalytic degradation performance and reaction mechanism

Benefit from the much-improved exciton dissociation and charge separation ability, SBOC-3 is expected to become an effective catalyst for electron-mediated photocatalytic system. In recent years, environmental pollution caused by drug abuse has received significant attention from all walks of life, involving antibiotic resistance and health threats caused by long-term consumption of food containing residual antibiotics [66,67]. Ciprofloxacin, a broad-spectrum fluoroquinolone antibacterial agent, has been widely found in hospital wastewater, sewage treatment plants, and surface water [68,69]. More worrisome is the long-term chronic toxicity of intermediate products produced after CIP degradation to environmental organisms [70]. The environmental concentrations of CIP under certain conditions are 5–20000 times higher than reported data [71]. Importantly, the photocatalytic degradation process of CIP can be dominated by  $^1\text{O}_2$  and  $\bullet\text{O}_2^-$  [72,73]. Herein, the photo-degradation capability of the obtained SBOC-3 catalyst for wastewater containing CIP under visible light ( $\lambda > 420$  nm) was evaluated. As shown in Fig. 7a, the self-degradation of CIP under irradiation was

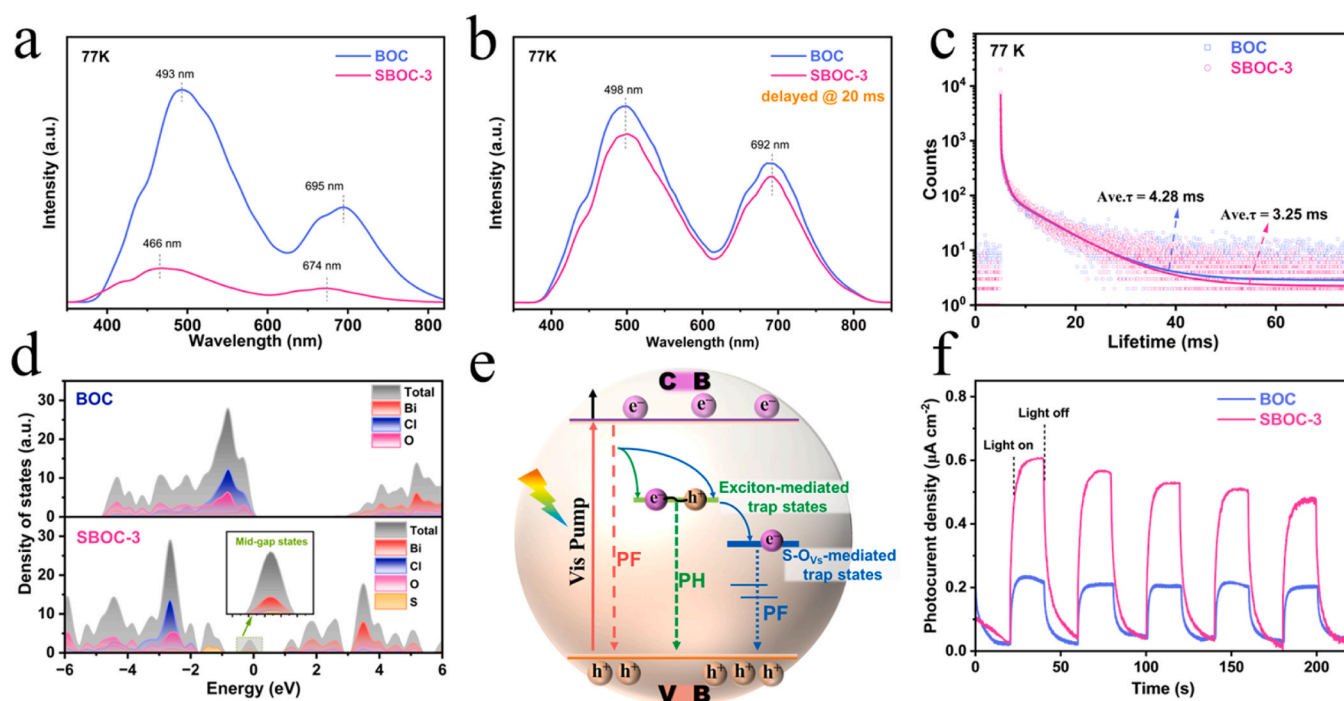


**Fig. 6.** Steady-state (a) prompt fluorescence spectra and (b) phosphorescence spectra recorded at a delayed time of 20 ms over BOC and SBOC-3 samples under low-temperature (77 K). (c) Low-temperature (77 K) time-resolved PL spectra of BOC and SBOC-3 samples monitored at 498 nm. (d) Calculated density of states (DOS) of BOC and SBOC-3 (inset is the enlarged area from the red dashed rectangle). (e) Schematic illustration involving photophysical processes of exciton dissociation in the presence of vacancy mediated trap states. (f) Transient photocurrent of BOC and SBOC-3 under visible light.

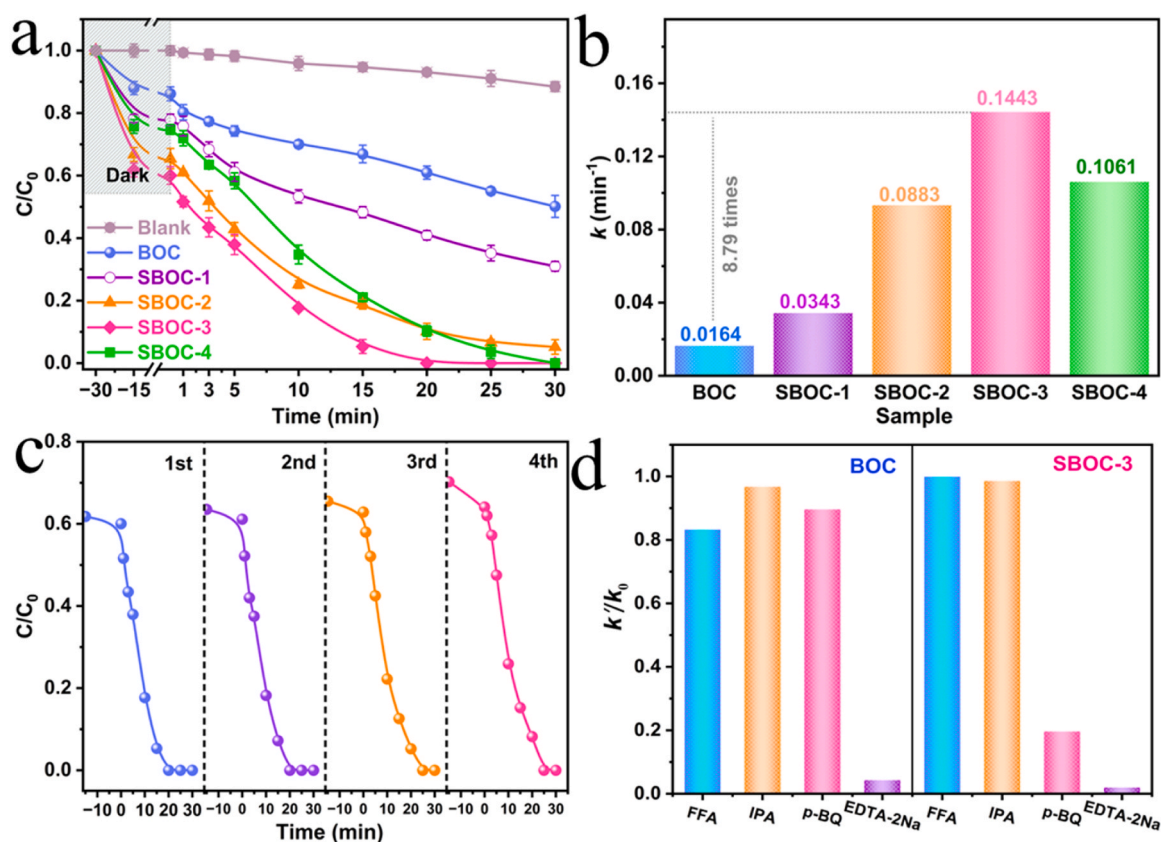


**Fig. 7.** Comparisons on the (a) photocatalytic degradation performance and (b) apparent reaction rates of CIP over the BOC and SBOC samples under visible light irradiation. (c) Recycling tests of SBOC-3 for the photodegradation of CIP. (d) The ratio of CIP degradation rate over BOC and SBOC-3 samples after the addition of various scavengers.

negligible. All samples got adsorption-desorption equilibrium within 30 min under dark conditions. The adsorption efficiency of SBOC samples were all enhanced due to the increase in the specific surface area and pore size distribution via S doping. Remarkably, 95% of the CIP was degraded by the SBOC-3 sample within 15 min under visible light irradiation, followed by complete removal at 20 min. In comparison, the pristine BOC sample showed low efficiency, with only 40% of CIP being removed within 20 min. The kinetic rate constant ( $k_{\text{obs}}$ ) of the samples was calculated using pseudo-first-order kinetics, where the  $k_{\text{obs}}$  of SBOC-3 ( $0.1443 \text{ min}^{-1}$ ) was approximately 8.8 times that of BOC ( $0.0164 \text{ min}^{-1}$ ), as depicted in Fig. 7b. It is evident that the SBOC-3 exhibited the optimal photocatalytic activity for CIP degradation among all as-fabricated samples, especially much higher than other BiOCl-based photocatalysts reported in previous studies (Table S2). We then evaluated the photodegradation behavior of SBOC-3 on CIP under different experimental conditions, including the adjustment of catalyst dosage, reaction concentration, and pH value (see Fig. S13 in the supplementary document). The specified reaction parameters manifested apparent impacts on removal performance. As for the effect of pH, it has been reported that CIP is most stable in reaction solutions with pH around 4.0, because its carboxyl group is not ionized and the basic nitrogen is complete protonation [74,75]. Additionally, the pH values of most pharmaceutical preparations and hospital sewage are typically between 3.5 and 5.5 and 6.4–9, respectively [76,77]. Impressively, the prepared SBOC-3 exhibited excellent degradation performance for CIP over a wide pH range of 2.5–9.33, with the highest degradation rate maintained under acidic environment ( $0.2689 \text{ min}^{-1}$  for 2.50 and  $0.2787 \text{ min}^{-1}$  for 3.91). In addition to CIP, SBOC-3 could also effectively remove various typical organic pollutants, including TC, SMX, and BPA (Fig. S14). Next, the remarkable stability and durability of the SBOC-3 samples was observed in cycle experiments. After reused for four cycles, the photodegradation efficiency of CIP hardly decreased for SBOC-3 (Fig. 7c). As displayed in Fig. S15, the XRD patterns and SEM images showed no obvious changes in the crystal structure and morphology of the SBOC-3 sample after the reaction. The above comprehensive results highlight the terrific photocatalytic performance of the SBOC-3 and its potential for treating practical water pollution.

A series of quenching experiments were conducted to further investigate the contribution of different active species in BOC and SBOC-3 during the CIP photodegradation [78]. As shown in Fig. 7d and Fig. S16, the addition of EDTA-2Na and p-BQ dramatically inhibited the CIP degradation activity, indicating that  $\text{h}^+$  and  $\bullet\text{O}_2^-$  were the main species involved in photocatalytic oxidation over SBOC-3. By contrast, only  $\text{h}^+$  was the predominant active species over BOC. The addition of FFA as a  $^1\text{O}_2$  scavenger did not significantly affect the degradation performance, probably because CIP is not sensitive to  $^1\text{O}_2$  (for BOC) or the yield of  $^1\text{O}_2$  was too low (for SBOC-3).

Subsequently, to further disclose the mechanism of the enhanced photocatalytic performance, we investigate the electronic structure of BOC and S-doped BOC samples via DFT calculations. Two geometric configuration models of the as-prepared materials were constructed, including the introduction of  $\text{O}_{\text{vs}}$  in S-doped BOC model, as shown in Fig. S17. The visualization calculation results of 3D charge density difference and corresponding electron localization function (ELF) indicated that charges prefer to be depleted at Bi atoms and accumulate at Cl atoms. The direction of the electric field is therefore from  $[\text{Bi}_2\text{O}_2]$  slice to  $[\text{Cl}]$  slice (Fig. S18 a and b). When the introduced S atom substituted the Cl atom, there was an uneven charge distribution between the slices, and the S atoms received more electrons from the Bi atoms (Fig. S18 c and d). This phenomenon proves that S doping triggers a more efficient charge transfer, thereby increasing the intrinsic BIEF in BOC. In addition, the highest occupied molecular orbital (HOMO) and the lowest unoccupied molecular orbital (LUMO) in the pristine BOC model were evenly distributed, with the former mainly occupied by Bi and Cl atoms, while the latter concentrated on Bi atoms, and the charge distribution of the two displayed a certain symmetry (Fig. S17). The presence of S dopant

and  $\text{O}_{\text{vs}}$  broke the original balance and caused significant influences on the direction and intensity of the charge density distribution of LUMO and HOMO. As shown in Fig. 8, HOMO and LUMO were simultaneously concentrated on the position of S atoms, which was consistent with the calculated results of DOS (Fig. 6d), as S doping led to the appearance of a defect state energy level. Moreover, LUMO was also occupied by the  $\text{O}_{\text{vs}}$  significantly that acts as the electron donor. Noticeably, S-doped BOC possessed more active sites for driving the photodegradation reactions, since its lobes of HOMO-LUMO were larger and more extensive than that of pristine BOC. The above DFT simulation results clearly revealed that doping of S was conducive to enhancing the BIEF. When stimulated by light, S atoms can act as electron donors and acceptors to accelerate the rapid separation and transport of charge carriers.

It can be proven that both samples involved interfacial transfer of electrons and holes during the CIP degradation process. The BIEF perpendicular to positive  $[\text{Bi}_2\text{O}_2]$  slices and double negative  $[\text{Cl}]$  slices drives the movement of electrons and holes towards  $[\text{Bi}_2\text{O}_2]^{2+}$  slices and  $[\text{Cl}]^-$  slices, respectively [34,79]. The robust exciton dissociation and spatial charge separation capabilities in SBOC-3 endowed it with superb photocatalytic performance. Accordingly, the photocatalytic process of SBOC-3 under visible light irradiation was proposed (Fig. 9): Initially, the enhanced BIEF weakened the exciton binding energy, meanwhile the excitons were accelerated to dissociate into charge carriers and the recombination of carriers was restrained; Subsequently, the holes reaching the catalyst surface directly attacked organic pollutants, while the electrons eliminated pollutants by activating molecular oxygen toward the generation of  $\bullet\text{O}_2^-$  via a charge transfer process.

### 3.6. Degradation pathways of CIP

To evaluate the safety pathway of CIP degradation by SBOC-3, samples were collected at certain intervals of irradiation for LC-MS analysis to identify degradation intermediates. As the illumination time went by, the intensity of target  $m/z$  332 representing CIP rapidly decreases, accompanied by an increase in the abundance of intermediate products (Fig. S20). Based on the identification of active species and transformation products, several major pathways involved in CIP photodegradation were proposed, including photooxidation, defluorination, decarboxylation, and piperazine ring cleavage (Fig. 10). The corresponding MS spectra were illustrated in Supporting Information (Fig. S21).

**Pathway I** mainly involved the opening of the piperazine ring. The  $\text{h}^+$  and  $\bullet\text{O}_2^-$  generated by SBOC-3 attacked the piperazine ring and excessively oxidized the C–N bond to form the dialdehyde derivative of  $m/z$  362 (P1). Then, the N atoms in P1 ( $m/z$  362) was attacked by  $\text{h}^+$ , resulting in the continuous loss of –CO group, and then two isomeric monoaldehydes were formed with  $m/z$  334 (P2/P2'), where the carbonyl group (–CHO) was retained on the N atom of aniline and alkylamine respectively [80]. The detected small molecule intermediate P3 ( $m/z$  185) could be further oxidized by P2/P2', meanwhile the loss of formaldehyde group in P2' ( $m/z$  = 334) caused the formation of the intermediate P4 with  $m/z$  306 [70]. The amino groups of P4 ( $m/z$  306) were further oxidized by  $\bullet\text{O}_2^-$  or destroyed by quinolone moiety, leading to the formation of P5 with  $m/z$  = 291 and P6 with  $m/z$  = 281, respectively [81]. In addition, the loss of secondary amine side chain and formaldehyde in P4 ( $m/z$  306) and the decarboxylation of P5 ( $m/z$  291) both pointed to the production of product P7 ( $m/z$  263). After decarboxylation, P7 ( $m/z$  263) was degraded to P8 ( $m/z$  218), followed by the structure was completely broke and transformed into the small molecule P11 ( $m/z$  126) [82,83]. In **pathway II**, the CIP molecule first suffered the loss of cyclopropane ring and generated product P6' ( $m/z$  291) [53]. Attributed to the piperazine ring cleavage, P6' ( $m/z$  291) was converted into P9 with  $m/z$  = 265 [84]. P9 ( $m/z$  265) completely lost its carboxyl group and piperazine ring to further formed product P10 ( $m/z$  163). Under the attack by  $\bullet\text{O}_2^-$ , the quinolone ring of P10 ( $m/z$  163) was removed, resulting in the formation of P11 ( $m/z$  126). **Pathway III** is



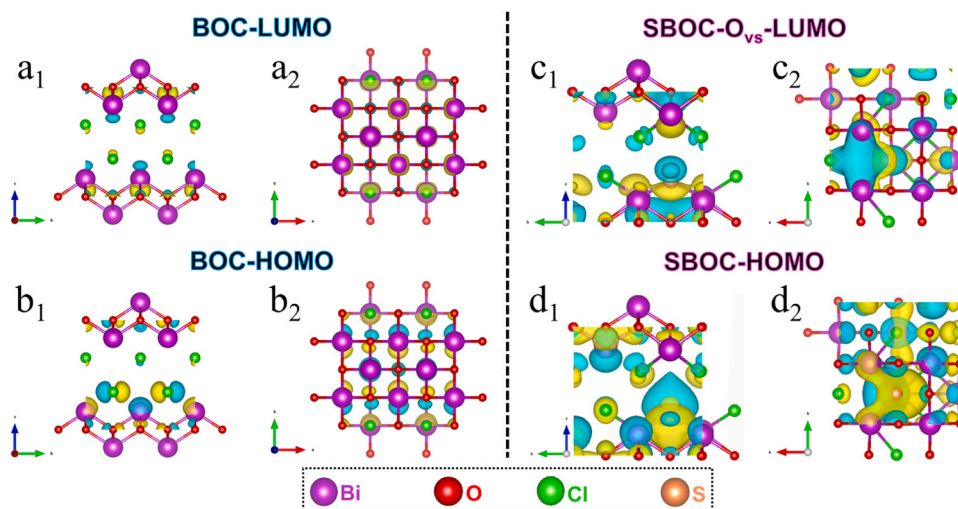


Fig. 8. (a, c) The lowest unoccupied molecular orbital (LUMO) and (b, d) the highest occupied molecular orbital (HOMO) of BOC and SBOC, respectively.

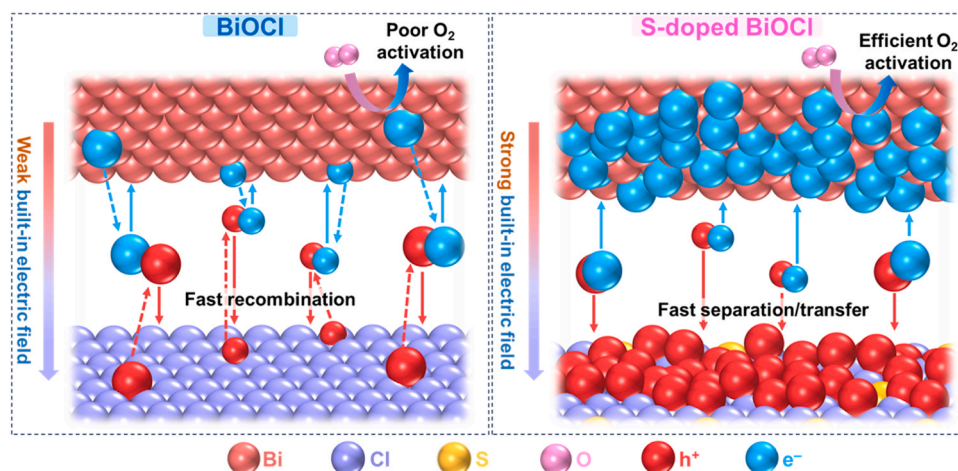


Fig. 9. Schematic illustration of the separation and migration of photogenerated charge carriers in the pristine and S-doped BOC.

dominated by the defluorination process. Due to the elimination of the fluorine group via  $\bullet\text{O}_2^-$ , the CIP molecule was first converted to P12 with  $m/z = 313$  [81]. Furthermore, the piperazine ring was attacked and then cracked to form P13 ( $m/z$  245), followed by the loss of  $-\text{CO}$  group to form P14 ( $m/z$  217). The loss of  $-\text{OH}$  groups in P14 ( $m/z$  217) resulted in the production of P15 ( $m/z$  174). The ultimate step in this pathway was the transformation of the product P16 with  $m/z = 147$  through the loss of amino group from the previous intermediate and the cleavage of the quinolone ring. As regards another possible **pathway IV**, the F atoms in CIP molecule were substituted by  $-\text{OH}$  since the resonance effect, generating the isomer P1' ( $m/z$  362) of P1 ( $m/z$  362) [85], which was further converted to P2'' ( $m/z$  334) by hydroxylation. After hydrolysis and free radical attack, P2'' ( $m/z$  334) underwent dehydroxylation and quinolone ring cleavage to form P17 ( $m/z$  285) and P18 ( $m/z$  295), respectively [86]. In the final stage, the intermediate products can be further transformed by SBOC-3 into short chain organic molecules and until mineralized into inorganic matters, such as  $\text{CO}_2$  and  $\text{H}_2\text{O}$ . The superior TOC removal efficiency of SBOC-3 verified this (Fig. S22).

According to the above results and previous reports, we have found that the main conversion reaction during CIP degradation occurs on the substituents without destroying the integrity of core quinolone framework, which tends to result in conversion products more biologically active [87]. In this regard, the ecotoxicity of CIP and its transformation

products on various species (such as fish, daphnid, and green algae) was further predicted via using ECOSAR Application 2.2 model [88]. The degree of toxicity was classified into four levels based on the Globally Harmonized System of Classification and Labelling of Chemicals (Table S3). As depicted in Table S4 and Fig. 11, the overall acute and chronic toxicity of transformation products was effectively curbed, while a few products exhibited higher toxicity, implying potential environmental risks. Specifically, the products obtained from **pathway I** were basically non-toxic, and the conversion reaction was dominated by the cleavage/substitution of the piperazine ring or the cleavage of the cyclopropyl group [82]. A similar situation occurred in the first one or two products of **pathways II to IV**, regardless of whether the F group has been removed. This phenomenon is closely related to changes in spatial and electrostatic properties. Differently, when the carboxyl group on the quinolone ring was substituted by hydroxyl or even removed, the toxicity of the obtained products would dramatically increase, such as the transformation of P9 to P10, P13 to P14, and P1' to P2'', etc. This may be due to the products transformed by the hydroxylation and breakage of the substituents were easier penetrated into cells. Especially, the unhindered amino groups ( $\text{R-NH}$  and  $\text{R-NH}_2$ ) in P8, P10, P11, P15, and P16 also enhanced their electronegativity, resulting in much higher toxicity than CIP [87]. Fortunately, given that the major active species generated by SBOC-3 were  $\text{h}^+$  and  $\bullet\text{O}_2^-$ , decarboxylation and hydroxylation were secondary pathways in the conversion reaction.

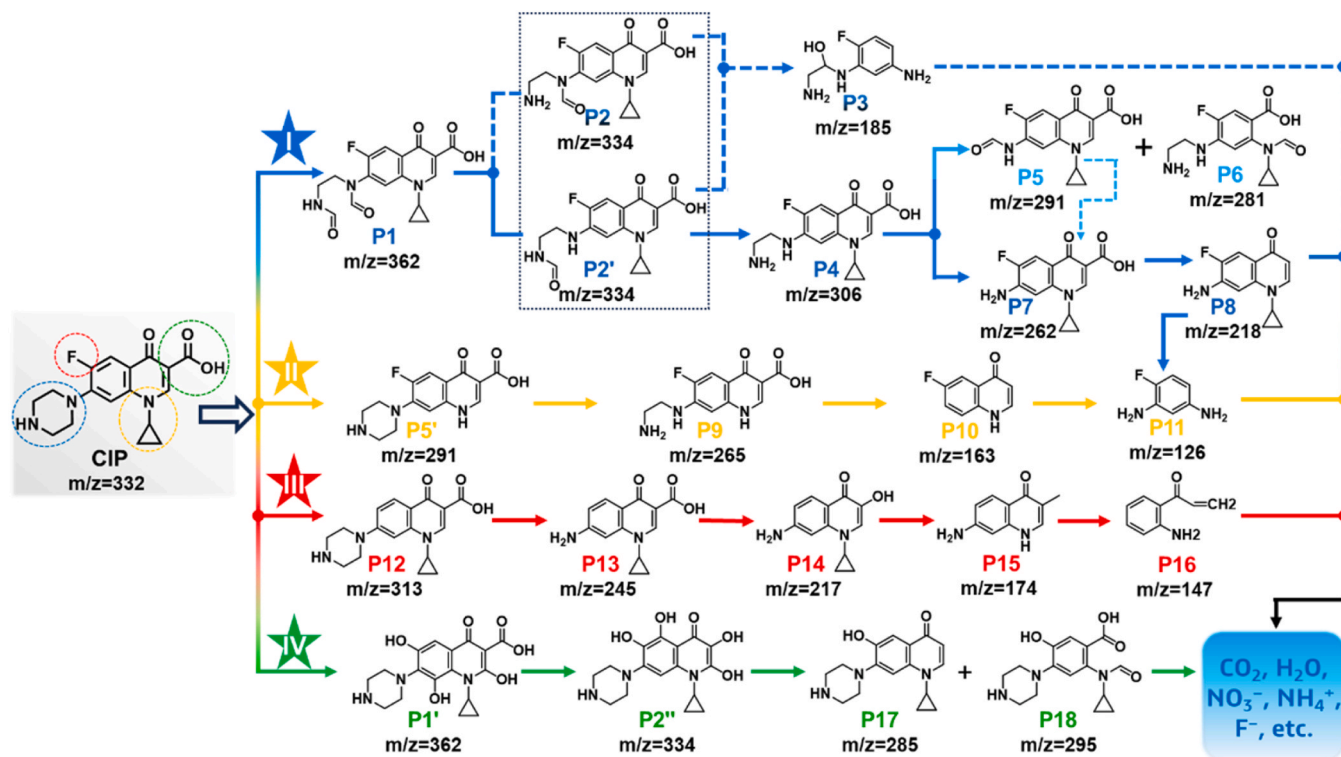


Fig. 10. Proposed photocatalytic degradation pathways of CIP over SBOC-3 sample under visible light.

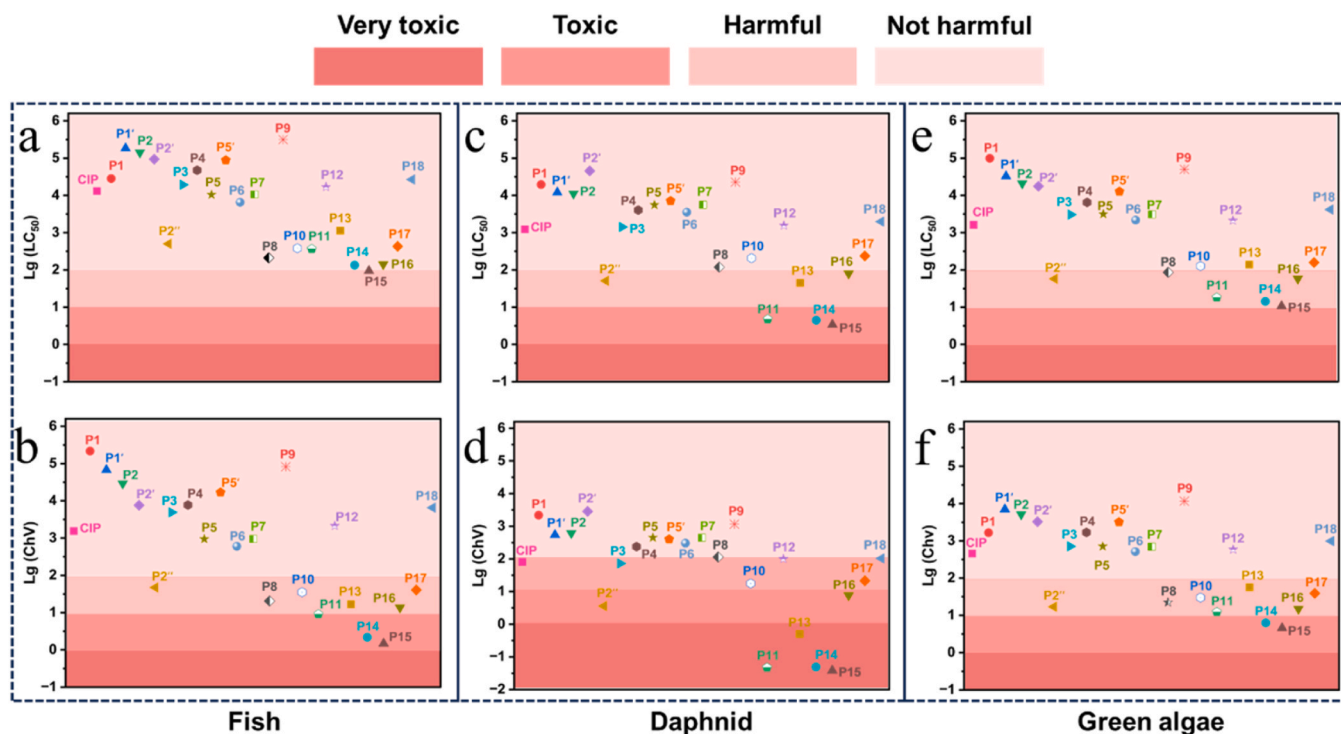


Fig. 11. Predicted acute and chronic toxicities of CIP and its transformation products.

Most of these toxic intermediates are small molecule compounds. Additionally, the products caused by hydroxyl radical attacks would also be rapidly converted into small molecule compounds due to their unstable structure [82]. Considering the reaction mechanism mentioned above, the toxicity of CIP can be diminished by the transformed products.

#### 4. Conclusions

In this work, we have demonstrated that S doping endowed BiOCl with remarkable photocatalytic activity, enabling the promotion of exciton dissociation for efficient activation of molecular oxygen toward deeply oxidizing CIP and other various antibiotics. Under visible light

irradiation, the as-fabricated SBOC-3 sample completely degrade CIP within 20 min, which was 8.8 times the degradation rate of BOC. In conclusion, the introduction of S not only increased the specific surface area to provide more active site, but also boosted the BIEF of BOC, which accelerated the separation and migration of carriers. Furthermore, S doping regulated the dissociation of excitons in BOC, resulting in a two-fold increase in electron concentration in BOC matrix. Compared to pristine BOC, more charge carriers in SBOC-3 would migrate from the bulk to the surface. Additionally, the increased the specific surface area of SBOC-3 could also better adsorb molecular oxygen and organic pollutants. On the one hand, the organic pollutants adsorbed on the surface active sites would be directly oxidized by holes. On the other hand, electrons could sharply activate the adsorbed  $O_2$  and selectively generate  $\bullet O_2^-$  via charge transfer. Through understanding the influence of the BIEF on excitonic effect in BiOCl, a typical 2D semiconductor, we can better explore the photocatalytic process in which excitons participate. Moreover, given such powerful  $O_2$  activation capability, this work provides encouraging insights into how to rationally design high-performance photocatalysts employing doping engineering.

### CRediT authorship contribution statement

**Chenyu Zhang:** Writing – original draft, Methodology, Formal analysis, Data curation, Conceptualization, Validation. **Yaocheng Deng:** Formal analysis, Writing – review & editing, Methodology. **Qiongfeng Wan:** Data curation, Formal analysis. **Hao Zeng:** Data curation, Visualization. **Hou Wang:** Methodology, Writing – review & editing. **Hanbo Yu:** Investigation, Conceptualization. **Haoliang Pang:** Formal analysis, Validation. **Wei Zhang:** Investigation. **Xingzhong Yuan:** Writing – review & editing. Funding acquisition, Supervision. **Jinhui Huang:** Funding acquisition, Supervision, Resources, Writing – review & editing.

### Declaration of Competing Interest

The authors declare that they have no known competing financial interests or personal relationships that could have appeared to influence the work reported in this paper.

### Data Availability

Data will be made available on request.

### Acknowledgments

This work was financially supported by the National Natural Science Foundation of China (51739004, 21776066, 52270156), the Natural Science Foundation of Hunan province (2022JJ40503), and the Training Program for Excellent Young Innovators of Changsha (kq2209015).

### Appendix A. Supporting information

Supplementary data associated with this article can be found in the online version at [doi:10.1016/j.apcatb.2023.123557](https://doi.org/10.1016/j.apcatb.2023.123557).

### References

- [1] H. Yu, J. Huang, L. Jiang, L. Leng, K. Yi, W. Zhang, C. Zhang, X. Yuan, In situ construction of Sn-doped structurally compatible heterojunction with enhanced interfacial electric field for photocatalytic pollutants removal and  $CO_2$  reduction, *Appl. Catal. B: Environ.* 298 (2021), 120618.
- [2] J. Ji, R. Li, H. Zhang, Y. Duan, Q. Liu, H. Wang, Z. Shen, Highly selective photocatalytic reduction of  $CO_2$  to ethane over Au-O-Ce sites at micro-interface, *Appl. Catal. B: Environ.* 321 (2023), 122020.
- [3] C. Zhang, H. Wang, H. Yu, K. Yi, W. Zhang, X. Yuan, J. Huang, Y. Deng, G. Zeng, Single-atom catalysts for hydrogen generation: rational design, recent advances, and perspectives, *Adv. Energy Mater.* 12 (2022) 2200875.
- [4] L. Liu, J. Huang, H. Yu, J. Wan, L. Liu, K. Yi, W. Zhang, C. Zhang, Construction of  $MoO_3$  nanoparticles/g- $C_3N_4$  nanosheets 0D/2D heterojunction photocatalysts for enhanced photocatalytic degradation of antibiotic pollutant, *Chemosphere* 282 (2021), 131049.
- [5] A. Mills, R.H. Davies, D. Worsley, Water purification by semiconductor photocatalysis, *Chem. Soc. Rev.* 22 (1993) 417–425.
- [6] M.A. Fox, M.T. Dulay, Heterogeneous photocatalysis, *Chem. Rev.* 93 (1993) 341–357.
- [7] H. Xu, X. Liu, H. Li, L. Zhang,  $O_2$  activation and  $^1O_2$  generation over phosphate modified BiOCl for efficient photodegradation of organic pollutants, *Appl. Catal. B: Environ.* 314 (2022), 121520.
- [8] D. Zhang, P. Wang, J. Wang, Y. Li, Y. Xia, S. Zhan, Tailoring of electronic and surface structures boosts exciton-triggering photocatalysis for singlet oxygen generation, *Proc. Natl. Acad. Sci.* 118 (2021), e2114729118.
- [9] Z. Zhou, Z. Shen, C. Song, M. Li, H. Li, S. Zhan, Boosting the activation of molecular oxygen and the degradation of tetracycline over high loading Ag single atomic catalyst, *Water Res.* 201 (2021), 117314.
- [10] X. Xu, J. Wang, T. Chen, N. Yang, S. Wang, X. Ding, H. Chen, Deep insight into ROS mediated direct and hydroxylated dichlorination process for efficient photocatalytic sodium pentachlorophenate mineralization, *Appl. Catal. B: Environ.* 296 (2021), 120352.
- [11] Y. Shi, Z. Yang, L. Shi, H. Li, X. Liu, X. Zhang, J. Cheng, C. Liang, S. Cao, F. Guo, X. Liu, Z. Ai, L. Zhang, Surface boronizing can weaken the excitonic effects of BiOBr nanosheets for efficient  $O_2$  activation and selective NO oxidation under visible light irradiation, *Environ. Sci. Technol.* 56 (2022) 14478–14486.
- [12] S. Wang, T. Li, X. Cheng, R. Zhu, Y. Xu, Regulating the concentration of dissolved oxygen to achieve the directional transformation of reactive oxygen species: A controllable oxidation process for ciprofloxacin degradation by calcined CuCoFe-LDH, *Water Res.* 233 (2023), 119744.
- [13] T. Gan, J. Yang, D. Morris, X. Chu, P. Zhang, W. Zhang, Y. Zou, W. Yan, S.-H. Wei, G. Liu, Electron donation of non-oxide supports boosts  $O_2$  activation on nano-platinum catalysts, *Nat. Commun.* 12 (2021) 2741.
- [14] P. Cudazzo, L. Sponza, C. Giorgetti, L. Reining, F. Sottile, M. Gatti, Exciton band structure in two-dimensional materials, *Phys. Rev. Lett.* 116 (2016), 066803.
- [15] S. Bai, X. Li, Q. Kong, R. Long, C. Wang, J. Jiang, Y. Xiong, Toward enhanced photocatalytic oxygen evolution: synergetic utilization of plasmonic effect and schottky junction via interfacing facet selection, *Adv. Mater.* 27 (2015) 3444–3452.
- [16] C. Mongin, S. Garakyaraghi, N. Razgoniaeva, M. Zamkov, F.N. Castellano, Direct observation of triplet energy transfer from semiconductor nanocrystals, *Science* 351 (2016) 369–372.
- [17] Y.-Z. Ma, L. Valkunas, S.L. Dexheimer, S.M. Bachilo, G.R. Fleming, Femtosecond spectroscopy of optical excitations in single-walled carbon nanotubes: evidence for exciton-exciton annihilation, *Phys. Rev. Lett.* 94 (2005), 157402.
- [18] Y. Qian, D. Li, Y. Han, H.-L. Jiang, Photocatalytic molecular oxygen activation by regulating excitonic effects in covalent organic frameworks, *J. Am. Chem. Soc.* 142 (2020) 20763–20771.
- [19] J. Li, H. Li, G. Zhan, L. Zhang, Solar water splitting and nitrogen fixation with layered bismuth oxyhalides, *Acc. Chem. Res.* 50 (2017) 112–121.
- [20] H. Wang, S. Chen, D. Yong, X. Zhang, S. Li, W. Shao, X. Sun, B. Pan, Y. Xie, Giant electron-hole interactions in confined layered structures for molecular oxygen activation, *J. Am. Chem. Soc.* 139 (2017) 4737–4742.
- [21] H. Wang, D. Yong, S. Chen, S. Jiang, X. Zhang, W. Shao, Q. Zhang, W. Yan, B. Pan, Y. Xie, Oxygen-vacancy-mediated exciton dissociation in biobr for boosting charge-carrier-involved molecular oxygen activation, *J. Am. Chem. Soc.* 140 (2018) 1760–1766.
- [22] Y. Shi, G. Zhan, H. Li, X. Wang, X. Liu, L. Shi, K. Wei, C. Ling, Z. Li, H. Wang, C. Mao, X. Liu, L. Zhang, Simultaneous manipulation of bulk excitons and surface defects for ultrastable and highly selective  $CO_2$  photoreduction, *Adv. Mater.* 33 (2021) 2100143.
- [23] F. Paquin, J. Rivnay, A. Salleo, N. Stingelin, C. Silva-Acuña, Multi-phase microstructures drive exciton dissociation in neat semicrystalline polymeric semiconductors, *J. Mater. Chem. C* 3 (2015) 10715–10722.
- [24] F. Paquin, G. Latini, M. Sakowicz, P.-L. Karsenti, L. Wang, D. Beljonne, N. Stingelin, C. Silva, Charge separation in semicrystalline polymeric semiconductors by photoexcitation: is the mechanism intrinsic or extrinsic? *Phys. Rev. Lett.* 106 (2011), 197401.
- [25] H. Wang, X. Sun, D. Li, X. Zhang, S. Chen, W. Shao, Y. Tian, Y. Xie, Boosting hot-electron generation: exciton dissociation at the order-disorder interfaces in polymeric photocatalysts, *J. Am. Chem. Soc.* 139 (2017) 2468–2473.
- [26] X. Sun, X. Luo, X. Zhang, J. Xie, S. Jin, H. Wang, X. Zheng, X. Wu, Y. Xie, Enhanced superoxide generation on defective surfaces for selective photooxidation, *J. Am. Chem. Soc.* 141 (2019) 3797–3801.
- [27] H. Li, F. Qin, Z. Yang, X. Cui, J. Wang, L. Zhang, New reaction pathway induced by plasmon for selective benzyl alcohol oxidation on biocl possessing oxygen vacancies, *J. Am. Chem. Soc.* 139 (2017) 3513–3521.
- [28] F. Li, X. Yue, D. Zhang, J. Fan, Q. Xiang, Targeted regulation of exciton dissociation in graphitic carbon nitride by vacancy modification for efficient photocatalytic  $CO_2$  reduction, *Appl. Catal. B: Environ.* 292 (2021), 120179.
- [29] Y.-Z. Chen, Z.U. Wang, H. Wang, J. Lu, S.-H. Yu, H.-L. Jiang, Singlet oxygen-engaged selective photo-oxidation over pt nanocrystals/porphyrinic MOF: the roles of photothermal effect and Pt electronic state, *J. Am. Chem. Soc.* 139 (2017) 2035–2044.
- [30] J. Tang, X. Li, Y. Ma, K. Wang, Z. Liu, Q. Zhang, Boosting exciton dissociation and charge transfer by regulating dielectric constant in polymer carbon nitride for  $CO_2$  photoreduction, *Appl. Catal. B: Environ.* 327 (2023), 122417.



- [31] W. Shao, L. Wang, H. Wang, Z. Zhao, X. Zhang, S. Jiang, S. Chen, X. Sun, Q. Zhang, Y. Xie, Efficient exciton dissociation in heterojunction interfaces realizing enhanced photoresponsive performance, *J. Phys. Chem. Lett.* 10 (2019) 2904–2910.
- [32] R. Zhou, D. Zhang, P. Wang, Y. Huang, Regulation of excitons dissociation in AgI/Bi<sub>2</sub>O<sub>3</sub>Br for advanced reactive oxygen species generation towards photodegradation, *Appl. Catal. B: Environ.* 285 (2021), 119820.
- [33] Y. Jin, F. Li, T. Li, X. Xing, W. Fan, L. Zhang, C. Hu, Enhanced internal electric field in S-doped BiOBr for intercalation, adsorption and degradation of ciprofloxacin by photoinitiation, *Appl. Catal. B: Environ.* 302 (2022).
- [34] J. Li, L. Cai, J. Shang, Y. Yu, L. Zhang, Giant enhancement of internal electric field boosting bulk charge separation for photocatalysis, *Adv. Mater.* 28 (2016) 4059–4064.
- [35] Q. Zhang, T. Hou, H. Shen, C. Guan, L. Duan, X. Zhao, Optical and photocatalytic properties of S doped BiOCl nanosheets with tunable exposed {001} facets and band gap, *Appl. Surf. Sci.* 600 (2022), 154020.
- [36] J. Xiong, H.-Y. Zeng, S. Xu, J.-F. Peng, F.-Y. Liu, L.-H. Wang, Enhancing the intrinsic properties of flower-like BiOI by S-doping toward excellent photocatalytic performances, *J. Mater. Sci. Technol.* 118 (2022) 181–189.
- [37] Q. Li, J. Ren, Y.-J. Hao, Y.-L. Li, X.-J. Wang, Y. Liu, R. Su, F.-T. Li, Insight into reactive species-dependent photocatalytic toluene mineralization and deactivation pathways via modifying hydroxyl groups and oxygen vacancies on BiOCl, *Appl. Catal. B: Environ.* 317 (2022), 121761.
- [38] G. Kresse, J. Furthmüller, Efficient iterative schemes for ab initio total-energy calculations using a plane-wave basis set, *Phys. Rev. B* 54 (1996) 11169–11186.
- [39] G. Kresse, J. Furthmüller, Efficiency of ab-initio total energy calculations for metals and semiconductors using a plane-wave basis set, *Comput. Mater. Sci.* 6 (1996) 15–50.
- [40] J.P. Perdew, K. Burke, M. Ernzerhof, Generalized gradient approximation made simple, *Phys. Rev. Lett.* 77 (1996) 3865–3868.
- [41] H.J. Monkhorst, J.D. Pack, Special points for Brillouin-zone integrations, *Phys. Rev. B* 13 (1976) 5188–5192.
- [42] Z. Luo, H. Li, H. Shu, K. Wang, J. Xia, Y. Yan, Synthesis of BaMoO<sub>4</sub> nestlike nanostructures under a new growth mechanism, *Cryst. Growth Des.* 8 (2008) 2275–2281.
- [43] J.C. Sczancoski, M.D.R. Bomio, L.S. Cavalcante, M.R. Joya, P.S. Pizani, J.A. Varela, E. Longo, M.S. Li, J.A. Andrés, Morphology and blue photoluminescence emission of PbMoO<sub>4</sub> processed in conventional hydrothermal, *J. Phys. Chem. C* 113 (2009) 5812–5822.
- [44] D.C. Ghosh, R. Biswas, Theoretical calculation of absolute radii of atoms and ions. Part 1. The atomic radii, *Int. J. Mol. Sci.* (2002) 87–113.
- [45] J.C. Slater, Atomic radii in crystals, *J. Chem. Phys.* 41 (1964) 3199–3204.
- [46] Y. Bu, H. Li, W. Yu, Y. Pan, L. Li, Y. Wang, L. Pu, J. Ding, G. Gao, B. Pan, Peroxydisulfate activation and singlet oxygen generation by oxygen vacancy for degradation of contaminants, *Environ. Sci. Technol.* 55 (2021) 2110–2120.
- [47] J. Zhang, L. Zhang, X. Shen, P. Xu, J. Liu, Synthesis of BiOBr/WO<sub>3</sub> p–n heterojunctions with enhanced visible light photocatalytic activity, *CrystEngComm* 18 (2016) 3856–3865.
- [48] P. Wang, J. Wang, X. Wang, H. Yu, J. Yu, M. Lei, Y. Wang, One-step synthesis of easy-recycling TiO<sub>2</sub>-rGO nanocomposite photocatalysts with enhanced photocatalytic activity, *Appl. Catal. B: Environ.* 132–133 (2013) 452–459.
- [49] J. Huang, L. Zhu, G. Zeng, L. Shi, Y. Shi, K. Yi, X. Li, Recovery of Cd(II) and surfactant in permeate from MEUF by foam fractionation with anionic-nonionic surfactant mixtures, *Colloids Surf. A: Physicochem. Eng. Asp.* 570 (2019) 81–88.
- [50] Y. Shi, X. Xiong, S. Ding, X. Liu, Q. Jiang, J. Hu, In-situ topotactic synthesis and photocatalytic activity of plate-like BiOCl/2D networks Bi<sub>2</sub>S<sub>3</sub> heterostructures, *Appl. Catal. B: Environ.* 220 (2018) 570–580.
- [51] Z. Xing, J. Hu, M. Ma, H. Lin, Y. An, Z. Liu, Y. Zhang, J. Li, S. Yang, From one to two: in situ construction of an ultrathin <sup>2</sup>D–<sup>2</sup>D closely bonded heterojunction from a single-phase monolayer nanosheet, *J. Am. Chem. Soc.* 141 (2019) 19715–19727.
- [52] C.-Y. Wang, X. Zhang, H.-B. Qiu, G.-X. Huang, H.-Q. Yu, Bi<sub>24</sub>O<sub>31</sub>Br<sub>10</sub> nanosheets with controllable thickness for visible-light-driven catalytic degradation of tetracycline hydrochloride, *Appl. Catal. B: Environ.* 205 (2017) 615–623.
- [53] F. Guo, H. Zhang, H. Li, Z. Shen, Modulating the oxidative active species by regulating the valence of palladium cocatalyst in photocatalytic degradation of ciprofloxacin, *Appl. Catal. B: Environ.* 306 (2022), 121092.
- [54] H. Yu, J. Huang, L. Jiang, Y. Shi, K. Yi, W. Zhang, J. Zhang, H. Chen, X. Yuan, Enhanced photocatalytic tetracycline degradation using N-CQDs/OV-BiOBr composites: unraveling the complementary effects between N-CQDs and oxygen vacancy, *Chem. Eng. J.* 402 (2020), 126187.
- [55] L. Shi, J. Huang, L. Zhu, Y. Shi, K. Yi, X. Li, Role of concentration polarization in cross flow micellar enhanced ultrafiltration of cadmium with low surfactant concentration, *Chemosphere* 237 (2019), 124859.
- [56] P. Li, Z. Zhou, Q. Wang, M. Guo, S. Chen, J. Low, R. Long, W. Liu, P. Ding, Y. Wu, Y. Xiong, Visible-light-driven nitrogen fixation catalyzed by Bi<sub>5</sub>O<sub>7</sub>Br nanostructures: enhanced performance by oxygen vacancies, *J. Am. Chem. Soc.* 142 (2020) 12430–12439.
- [57] H. Yu, J. Huang, L. Jiang, X. Yuan, K. Yi, W. Zhang, J. Zhang, H. Chen, Steering photo-excitons towards active sites: Intensified substrates affinity and spatial charge separation for photocatalytic molecular oxygen activation and pollutant removal, *Chem. Eng. J.* 408 (2021), 127334.
- [58] J. Li, G. Zhan, Y. Yu, L. Zhang, Superior visible light hydrogen evolution of Janus bilayer junctions via atomic-level charge flow steering, *Nature, Communications* 7 (2016) 11480.
- [59] T. Kanata, M. Matsunaga, H. Takakura, Y. Hamakawa, T. Nishino, F.H. Pollak, M. Cardona, D.E. Aspnes, Photorefectance characterization of built-in potential in MBE-produced As-grown GaAs surface, *Proc. SPIE* 1286 (1990) 56–65.
- [60] H. Wang, S. Jiang, S. Chen, D. Li, X. Zhang, W. Shao, X. Sun, J. Xie, Z. Zhao, Q. Zhang, Y. Tian, Y. Xie, Enhanced singlet oxygen generation in oxidized graphitic carbon nitride for organic synthesis, *Adv. Mater.* 28 (2016) 6940–6945.
- [61] C.L. Hawkins, M.J. Davies, Detection and characterisation of radicals in biological materials using EPR methodology, *Biochim. Et. Biophys. Acta (BBA) - Gen. Subj.* 1840 (2014) 708–721.
- [62] Y. Nosaka, A.Y. Nosaka, Generation and detection of reactive oxygen species in photocatalysis, *Chem. Rev.* 117 (2017) 11302–11336.
- [63] C. Schweitzer, R. Schmidt, Physical mechanisms of generation and deactivation of singlet oxygen, *Chem. Rev.* 103 (2003) 1685–1758.
- [64] Q. Yi, J. Ji, B. Shen, C. Dong, J. Liu, J. Zhang, M. Xing, Singlet oxygen triggered by superoxide radicals in a molybdenum cocatalytic fenton reaction with enhanced REDOX activity in the environment, *Environ. Sci. Technol.* 53 (2019) 9725–9733.
- [65] Y.V. Romanovskii, A. Gerhard, B. Schweitzer, U. Scherf, R.I. Personov, H. Bässler, Phosphorescence of  $\pi$ -conjugated oligomers and polymers, *Phys. Rev. Lett.* 84 (2000) 1027–1030.
- [66] C. Zhang, Y. Deng, J. Zheng, Y. Zhang, L. Yang, C. Liao, L. Su, Y. Zhou, D. Gong, L. Chen, A. Luo, The application of the QuEChERS methodology in the determination of antibiotics in food: a review, *TrAC Trends Anal. Chem.* 118 (2019) 517–537.
- [67] L. Shi, J. Huang, G. Zeng, L. Zhu, Y. Gu, Y. Shi, K. Yi, X. Li, Roles of surfactants in pressure-driven membrane separation processes: a review, *Environ. Sci. Pollut. Res.* 26 (2019) 30731–30754.
- [68] I. Senta, S. Terzic, M. Ahel, Occurrence and fate of dissolved and particulate antimicrobials in municipal wastewater treatment, *Water Res.* 47 (2013) 705–714.
- [69] J. Porras, C. Bedoya, J. Silva-Agreto, A. Santamaría, J.J. Fernández, R.A. Torres-Palma, Role of humic substances in the degradation pathways and residual antibacterial activity during the photodecomposition of the antibiotic ciprofloxacin in water, *Water Res.* 94 (2016) 1–9.
- [70] X. Van Doorslaer, K. Demeestere, P.M. Heynderickx, H. Van Langenhove, J. Dewulf, UV-A and UV-C induced photolytic and photocatalytic degradation of aqueous ciprofloxacin and moxifloxacin: reaction kinetics and role of adsorption, *Appl. Catal. B: Environ.* 101 (2011) 540–547.
- [71] A.F. Martins, T.G. Vasconcelos, D.M. Henriques, C.d.S. Frank, A. König, K. Kümmerer, Concentration of ciprofloxacin in Brazilian hospital effluent and preliminary risk assessment: a case study, *CLEAN Soil, Air, Water* 36 (2008) 264–269.
- [72] F. Wang, Y. Feng, P. Chen, Y. Wang, Y. Su, Q. Zhang, Y. Zeng, Z. Xie, H. Liu, Y. Liu, W. Lv, G. Liu, Photocatalytic degradation of fluoroquinolone antibiotics using ordered mesoporous g-C<sub>3</sub>N<sub>4</sub> under simulated sunlight irradiation: Kinetics, mechanism, and antibacterial activity elimination, *Appl. Catal. B: Environ.* 227 (2018) 114–122.
- [73] J. Guo, H. Sun, X. Yuan, L. Jiang, Z. Wu, H. Yu, N. Tang, M. Yu, M. Yan, J. Liang, Photocatalytic degradation of persistent organic pollutants by Co-Cl bond reinforced CoAl-LDH/Bi<sub>12</sub>O<sub>17</sub>Cl<sub>2</sub> photocatalyst: mechanism and application prospect evaluation, *Water Res.* 219 (2022), 118558.
- [74] K. Torniainen, S. Tammilehto, V. Ulvi, The effect of pH, buffer type and drug concentration on the photodegradation of ciprofloxacin, *Int. J. Pharm.* 132 (1996) 53–61.
- [75] J. Huang, Y. Yang, G. Zeng, Y. Gu, Y. Shi, K. Yi, Y. Ouyang, J. Hu, L. Shi, Membrane layers intensifying quorum quenching alginate cores and its potential for membrane biofouling control, *Bioresour. Technol.* 279 (2019) 195–201.
- [76] S. Das, S. Ghosh, A.J. Misra, A.J. Tamhankar, A. Mishra, C.S. Lundborg, S. K. Tripathy, Sunlight Assist. Photo Degrad. Ciprofloxacin Water Using Fe Doped ZnO Nanopart. Potential Public Health Appl. 15 (2018) 2440.
- [77] T.G. Vasconcelos, D.M. Henriques, A. König, A.F. Martins, K. Kümmerer, Photodegradation of the antimicrobial ciprofloxacin at high pH: Identification and biodegradability assessment of the primary by-products, *Chemosphere* 76 (2009) 487–493.
- [78] J. Wan, J. Huang, H. Yu, L. Liu, Y. Shi, C. Liu, Fabrication of self-assembled <sup>0</sup>D–<sup>2</sup>D Bi<sub>2</sub>MoO<sub>6</sub>-g-C<sub>3</sub>N<sub>4</sub> photocatalytic composite membrane based on PDA intermediate coating with visible light self-cleaning performance, *J. Colloid Interface Sci.* 601 (2021) 229–241.
- [79] J. Li, Y. Yu, L. Zhang, Bismuth oxyhalide nanomaterials: layered structures meet photocatalysis, *Nanoscale* 6 (2014) 8473–8488.
- [80] X. Hu, X. Hu, Q. Peng, L. Zhou, X. Tan, L. Jiang, C. Tang, H. Wang, S. Liu, Y. Wang, Z. Ning, Mechanisms underlying the photocatalytic degradation pathway of ciprofloxacin with heterogeneous TiO<sub>2</sub>, *Chem. Eng. J.* 380 (2020), 122366.
- [81] F. Chen, G.-X. Huang, F.-B. Yao, Q. Yang, Y.-M. Zheng, Q.-B. Zhao, H.-Q. Yu, Catalytic degradation of ciprofloxacin by a visible-light-assisted peroxymonosulfate activation system: performance and mechanism, *Water Res.* 173 (2020), 115559.
- [82] T. Paul, M.C. Dodd, T.J. Strathmann, Photolytic and photocatalytic decomposition of aqueous ciprofloxacin: Transformation products and residual antibacterial activity, *Water Res.* 44 (2010) 3121–3132.
- [83] T. Paul, P.L. Miller, T.J. Strathmann, Visible-light-mediated TiO<sub>2</sub> photocatalysis of fluoroquinolone antibacterial agents, *Environ. Sci. Technol.* 41 (2007) 4720–4727.
- [84] R. Zhang, C. Peng, Q. Wang, X. Zou, Q. Zhao, J. Wang, J. Zhang, L. Dong, X. Zhang, N. Gao, Degradation of ciprofloxacin in UV/NH<sub>2</sub>Cl process: kinetics, mechanism, pathways and DBPs formation, *Environ. Sci.: Water Res. Technol.* (2023).
- [85] V.D. Dang, J. Adorna, T. Annadurai, T.A.N. Bui, H.L. Tran, L.-Y. Lin, R.-A. Doong, Indirect Z-scheme nitrogen-doped carbon dot decorated Bi<sub>2</sub>MoO<sub>6</sub>/g-C<sub>3</sub>N<sub>4</sub>

- photocatalyst for enhanced visible-light-driven degradation of ciprofloxacin, *Chem. Eng. J.* 422 (2021), 130103.
- [86] H. Cao, L. Xu, J. Ma, X. Dong, Y. Li, Z. Yin, Y. Yang, Q. Wang, J. Han, J. Qiu, Z. Yang, Z. Song, Simultaneous enhancement of charge transfer and light absorption via construction of atom-sharing Bi/Bi<sub>3</sub>Ti<sub>2</sub>O<sub>8</sub>F:Yb<sup>3+</sup>,Er<sup>3+</sup> plasmonic heterojunctions for the efficient degradation of ciprofloxacin, *Sep. Purif. Technol.* 309 (2023), 123096.
- [87] M. Li, D. Wei, H. Zhao, Y. Du, Genotoxicity of quinolones: Substituents contribution and transformation products QSAR evaluation using 2D and 3D models, *Chemosphere* 95 (2014) 220–226.
- [88] H. Zhang, H. Quan, S. Yin, L. Sun, H. Lu, Unraveling the toxicity associated with ciprofloxacin biodegradation in biological wastewater treatment, *Environ. Sci. Technol.* 56 (2022) 15941–15952.